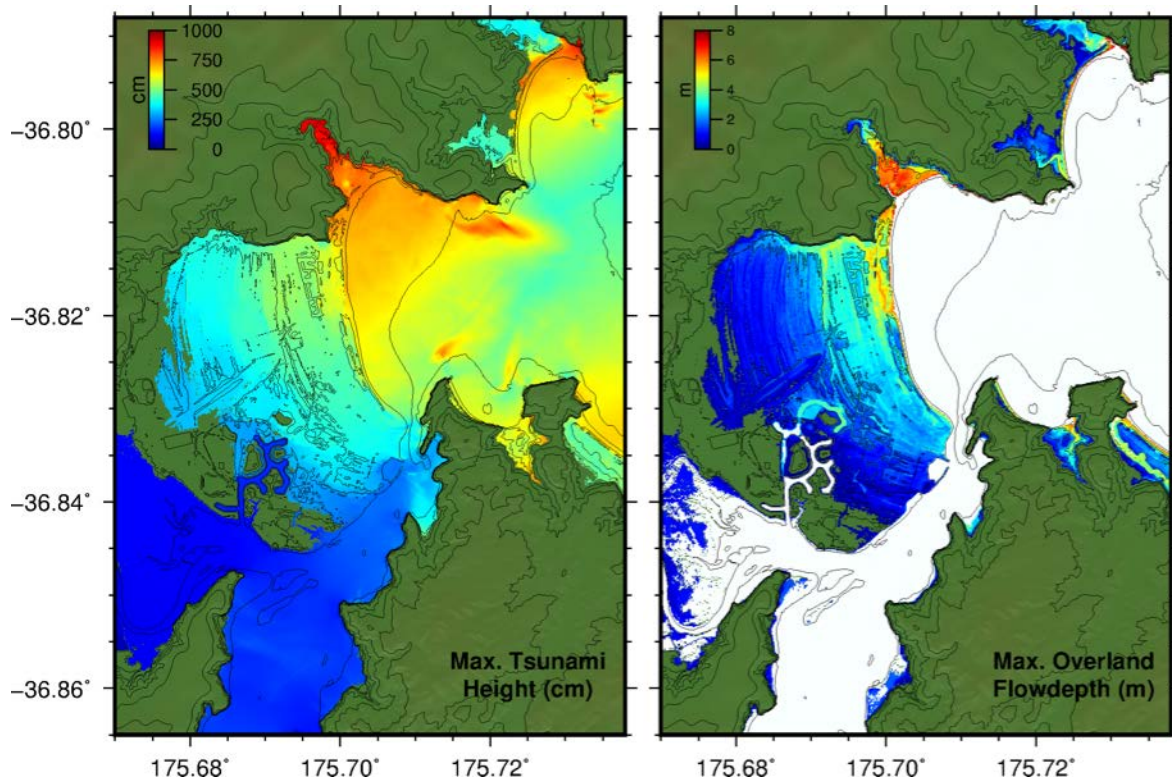


# Numerical Modelling of Tsunami Inundation in Whitianga, Mercury Bay, Hahei and Hot Water Beach, New Zealand



eCoast Limited  
Marine Consulting and Research  
P.O. Box 151  
Raglan, New Zealand

[jose@ecoast.co.nz](mailto:jose@ecoast.co.nz)

---

# Numerical Modelling of Tsunami Inundation in Whitianga, Mercury Bay, Hahei and Hot Water Beach, New Zealand

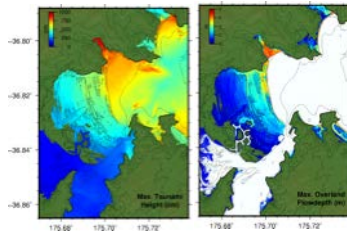
---

## Report Status

Version	Date	Status	Approved By:
V1	31-October-2016	DRAFT	JCB
V2	20-January-2017	FINAL	JCB

It is the responsibility of the reader to verify the currency of the version number of this report.

Jose C. Borrero Ph.D.



Cover Picture: Maximum tsunami height (left) and overland flood depth (right) along Buffalo Beach and Whitianga caused by tsunami source model 'Case 8' at High Tide (HT).

The information, including the intellectual property, contained in this report is confidential and proprietary to eCoast Limited. It may be used by the persons to whom it is provided for the stated purpose for which it is provided, and must not be imparted to any third person without the prior written approval of eCoast. eCoast Limited reserves all legal rights and remedies in relation to any infringement of its rights in respect of its confidential information.

© eCoast Limited 2017

## CONTENTS

<b>TABLE OF FIGURES</b> .....	<b>II</b>
<b>TABLE OF TABLES</b> .....	<b>V</b>
<b>1 INTRODUCTION</b> .....	<b>6</b>
1.1 REVIEW OF RECENT LITERATURE .....	8
1.2 MODELLING APPROACH.....	9
1.3 NUMERICAL MODELLING GRIDS.....	10
<b>2 TSUNAMI SOURCE MODELS</b> .....	<b>14</b>
2.1 NEAR SOURCE TONGA-KERMADEC TRENCH SCENARIOS .....	14
2.2 DISTANT SOURCE TSUNAMI MODELS.....	17
2.3 HISTORICAL SOUTH AMERICAN TSUNAMI SCENARIOS: 1960 VALDIVIA, 2010 MAULE AND 1868 ARICA EARTHQUAKES AND TSUNAMIS .....	18
2.4 ADDITIONAL SOUTH AMERICAN TSUNAMI SOURCES: PERU AND NORTHERN CHILE 20	
2.5 THE 2011 TOHOKU, JAPAN EARTHQUAKE AND TSUNAMI .....	22
<b>3 MODEL VALIDATION TO HISTORICAL EVENTS</b> .....	<b>24</b>
3.1 1960 CHILE TSUNAMI.....	24
3.2 THE TSUNAMIS OF 2010 AND 2011 .....	27
<b>4 MODEL RESULTS: TONGA-KERMADEC TRENCH SOURCES</b> .....	<b>31</b>
4.1 ARRIVAL TIMES.....	31
4.2 TSUNAMI HEIGHT .....	33
4.3 TSUNAMI CURRENT SPEEDS .....	40
<b>5 MODEL RESULTS: DISTANT SOURCE TSUNAMIS</b> .....	<b>42</b>
5.1 PROPAGATION MODELS .....	42
5.2 ARRIVAL TIMES.....	44
5.3 TSUNAMI HEIGHTS AND INUNDATION EXTENTS .....	44
5.4 TSUNAMI CURRENT SPEEDS .....	50
<b>6 MODEL SENSITIVITY: FRICTION COEFFICIENT</b> .....	<b>54</b>
<b>7 SUMMARY AND CONCLUSIONS</b> .....	<b>57</b>
<b>8 REFERENCES</b> .....	<b>59</b>

## TABLE OF FIGURES

Figure 1.1 Location map for the study sites in and around Whitianga and Mercury Bay, New Zealand. ....	7
Figure 1.2 The ComMIT propagation model database for tsunamis in the world's oceans. Insets show the details of the source zone discretization in to rectangular sub-faults. ....	9
Figure 1.3 Definition sketch for tsunami height, flow depth, runup and inundation distance. ....	10
Figure 1.4 coverage area of the different bathymetry data sets. Yellow: SRTM topography, Red and White: WRC supplied LiDAR, Aqua and Purple: LINZ digitised charts contours and sounding points. ....	10
Figure 1.5 The final numerical modelling grids: B grid (previous page top) at 150 m resolution. A) Buffalo Beach and the entrance to Whitianga Harbour B) An extended Buffalo Beach grid that include Cook's Beach and Wharekaho C) Hahei and D) Hot Water Beach at 10 m resolution. ....	13
Figure 2.1 Case 1, 2: 600 x 100 km fault 10.47 m average slip, M = 8.9. Case 3, 4: 600 x 100 km fault, 14.8 m average slip, M = 9. Note the change in the colour scale for cases 3 and 4. ....	15
Figure 2.2 Cases 5 and 6: 600 x 100 km fault, 20.9 m average slip, M = 9.1 .....	16
Figure 2.3 Case 7 (left) the Japan 2011 tsunami source positioned 200 km north of the East Cape (M = 8.8). Case 8 (right) the Japan 2011 tsunami source positioned at the southern end of the Tonga-Kermadec Trench (M=8.8).....	16
Figure 2.4 (left) Unit source segments used to define the 1960 Chilean Earthquake suite of events. (right) initial sea floor deformation at the source region. ....	18
Figure 2.5 Source segments and slip amounts used to model the 2010 Chile tsunami.....	19
Figure 2.6 Source segments used to model the 1868 Arica tsunami. A uniform slip amount of 39.6 m was applied to each segment.....	20
Figure 2.7 Three additional South American sources. Variants of the Fujii and Satake (2012) source for the 1960 Chile earthquake are positioned along the coast of Northern Chile and Southern Peru. ....	21
Figure 2.8 Fault segments used to construct the Central Peru tsunami source (left) and the initial deformation field used to initialise the tsunami model (right). ....	22
Figure 2.9 Source model used for the 2011 Tohoku tsunami, The amount of slip on each segment is indicated in the left panel, while the vertical deformation of the sea floor is shown on the right (image reproduced from Wei et al., 2012). ....	23
Figure 3.1 (top) The predicted tide on the day the 1960 Chile tsunami affected Whitianga. Important times are marked and noted. (bottom) Model results (red) for six source models compared to the predicted tide level (black). Blue dots indicate the modelled arrival time and the time when the worst effects were observed by the witnesses. ....	24
Figure 3.2 Modelled inundation for the 1960 Chilean event assuming mid tide conditions. Locations noted on the map are places where inundation effects were recorded in 1960. ....	25

Figure 3.3 Modelled inundation for the 1960 Chilean event assuming high tide conditions. Locations noted on the map are places where inundation effects were recorded in 1960. ....	26
Figure 3.4 Filtered tide gauge record of the 2010 Chile tsunami in Whitianga (bottom). Top plot shows the spectral content of the tsunami signal. ....	28
Figure 3.5 Filtered tide gauge record of the 2010 Chile tsunami in Whitianga (bottom). Top plot shows the spectral content of the tsunami signal. ....	28
Figure 3.6 Comparison of modelled to measured tsunami water levels at Whitianga from the 2010 Maule Chile tsunami.....	30
Figure 3.7 Comparison of modelled to measured tsunami water levels at Whitianga from the 2010 Maule Chile tsunami.....	30
Figure 4.1 Water level time series plots for the 8 sources just off shore of Buffalo Beach. ....	32
Figure 4.2 Tsunami wave heights produced offshore of the Coromandel Peninsula (red star) by identical tsunami sources positioned on each of the fault segments indicated in the panel on the left. Note that the strongest effects are the result of ruptures in the first 300 km north of the East Cape (segments 1, 2 and 3).....	33
Figure 4.3 Maximum computed tsunami heights over the regional grid for source TK 1 (left) and TK 2 (right). Tsunami heights along the Coromandel Peninsula and in the Bay of Plenty are noticeably higher from source TK 2 due to its more southerly position along the subduction zone. ....	33
Figure 4.4 Maximum computed tsunami height (left) and current speed (right) for scenarios TK 1 (top) and TK 2 (bottom) in Whitianga; each case run at HT.....	34
Figure 4.5 Maximum computed overland flow depths (left) and flow speeds (right) TK 1 (top) and TK 2 (bottom) in Whitianga; each case run at HT.....	35
Figure 4.6 Maximum computed tsunami height (left) and current speed (right) for scenarios TK 7 (top) and TK 8 (bottom) in Whitianga; each case run at HT.....	36
Figure 4.7 Maximum computed overland flow depths (left) and flow speeds (right) TK 7 (top) and TK 8 (bottom) in Whitianga; each case run at HT.....	37
Figure 4.8 Maximum computed tsunami heights (left) and current speeds (right) at Hahei (top) and Hot Water Beach (bottom) for the TK 8 HT scenario.....	38
Figure 4.9 Maximum computed tsunami flood depths above ground level (left) and overland flow speed (right) at Hahei (top) and Hot Water Beach (bottom) for the TK 8 HT scenario. ....	39
Figure 4.10 Computed maximum current speeds in Whitianga along Buffalo Beach from scenarios TK 1 (left) and TK 8 (right) at HT. ....	40
Figure 4.11 Time-current-threshold maps from scenarios TK1 (left) and TK8 (right) at Whitianga. ....	41
Figure 4.12 Current hazard zones for Mercury Bay. ....	41
Figure 5.1 Comparison between trans-Pacific propagation patterns for the 1960 Valdivia, Chile (top) and 2010 Maule Chile (bottom) tsunamis. ....	42

Figure 5.2 Comparison between trans-Pacific propagation patterns for the three hypothetical northern Chile scenarios: Chile North 1 (top) Chile North 2 (mid) and Chile North 3 (bottom). ..... 43

Figure 5.3 Modelled tsunami heights from the propagation model for the 1868 Arica scenario (left) and the Chile North 1 scenario (right). ..... 44

Figure 5.4 Modelled time series of water levels offshore of Buffalo Beach for each of the distant source scenarios. Measured tide gauge data plotted in red. .... 45

Figure 5.5 Modelled tsunami heights (left) and current speeds (right) from the 1960 Valdivia Chile scenario (FF1) at mid tide (top) and for the 2010 Maule Chile scenario (FF2) at mid tide (bottom) for Whitianga and Buffalo Beach. .... 46

Figure 5.6 Modelled tsunami heights (left) and current speeds (right) from the 1868 Arica scenario (FF3) (top) and the Chile North 1 (FF4) (bottom) at high tide for Whitianga and Buffalo Beach. .... 47

Figure 5.7 Modelled tsunami heights (top left) current speed (top right) flow depth (bottom left) and overland flow speed (bottom right) for the Southern Peru (FF 7) scenario at High tide ..... 48

Figure 5.8 Modelled tsunami heights (left) and current speeds (right) for Hahei (top) and Hot Water Beach (bottom) for the Southern Peru (Case 7) scenario. .... 49

Figure 5.9 Maximum modelled current speeds from the Arica 1868 (left) and Central Peru (right) scenarios for Whitianga at HT. .... 50

Figure 5.10 Time Current threshold maps for current speeds of 3 knots for the Chile 1960 (top left) Arica 1868 (top right), Chile North 1 (bottom left) and Central Peru (bottom right) at High tide in Whitianga and Buffalo Bay ..... 51

Figure 5.11 Current hazard zones for Whitianga showing areas where strong currents would be expected during large far-field tsunamis. .... 52

Figure 5.12 Maximum modelled current speeds as a function of the tsunami source. .... 53

Figure 6.1 Modelled water levels offshore of Buffalo Beach for the TK \* scenario at High Tide with three friction coefficients. .... 54

Figure 6.2 Modelled inundation extents and offshore current speeds in Whitianga as a function of different friction coefficients. .... 55

Figure 6.3 Modelled overland flow depths (left) overland flow speeds in Whitianga as a function of different friction coefficients. .... 56

**TABLE OF TABLES**

Table 2.1 Tsunami source models on the Tonga Kermadec Trench considered in this study.....	14
Table 2.2 Description of the distant source tsunami scenarios. ....	17
Table 2.3 Faults segment slip amounts for the 1960 Chilean tsunami.....	18
Table 3.1 Summary statistics for the Japan and Chile tsunamis on the Whitianga tide gauge. The arrival time is in hours after the earthquake. P2T = Peak to Trough. The timing of the maximum tsunami heights, maximum wave cycle and maximum sea levels are given in hours relative to tsunami arrival time. Data from Borrero and Greer (2013).....	27

# 1 INTRODUCTION

This report describes the assessment of tsunami effects resulting from regional and distant source earthquake along the northern Coromandel Peninsula. This report focuses on the effects in and around Whitianga and Mercury Bay and includes detailed assessments of the Whitianga township waterfront area, the upper harbour, Buffalo Beach, Cook's Beach, Wharekaho, Hahei and Hot Water Beach (Figure 1.1). Results presented here include the quantification of maximum and minimum tsunami wave heights, the extents of tsunami inundation and tsunami induced flood depths and the strength and duration of tsunami induced currents. The results from this study are intended to guide emergency management and evacuation planning activities. As such, this study focuses primarily on extreme tsunami scenarios in an effort to define likely maximum credible events for the purposes of planning evacuation routes and increasing public awareness. This report extends tsunami inundation and hazard studies previously completed by Borrero (2013, 2014, 2015). This work carries on from the work of Prasetya et al. (2008), who analysed near source and distant source tsunami inundation at Whitianga.

For the near source events, we consider a range of large magnitude ( $M > 8.5$ ) events located along the Tonga Kermadec trench, a subduction zone plate boundary between the Pacific and Australasian tectonic plates that extends from the east coast of the North Island to Tonga. For the distant source events, we consider only South American tsunamis for two reasons; firstly, sensitivity studies for Pacific Rim tsunamis conducted by Borrero et al. (2014) suggest that for a given earthquake size, tsunamis originating from South America have a larger impact in New Zealand than do tsunamis originating from most other parts of the Pacific Rim, and secondly, the South American Subduction Zone (SASZ) has a well-known history of producing very large earthquakes ( $>M8.5$ ) and is likely to produce another such event in coming decades. While the sensitivity study of Borrero et al. (2014) show that tsunamis originating from Central America produce somewhat larger tsunami heights in New Zealand than a South American source of equivalent magnitude, the subduction zone offshore of Central America has never produced an earthquake with sufficient magnitude to generate a trans-pacific tsunami. For this reason, tsunamis from Central America are not considered here, nor are large magnitude events from other parts of the Pacific Rim. Given the historical record and the results from Borrero et al. (2014) we assume that the cases modelled here represent maximum credible event for distant source tsunamis.

We use the current state-of-the art tsunami modelling tools (ComMIT: Titov et al. 2011) and the most recent scientific literature on the relevant tsunami source mechanisms. Model results are compared quantitatively and qualitatively to available historical information.

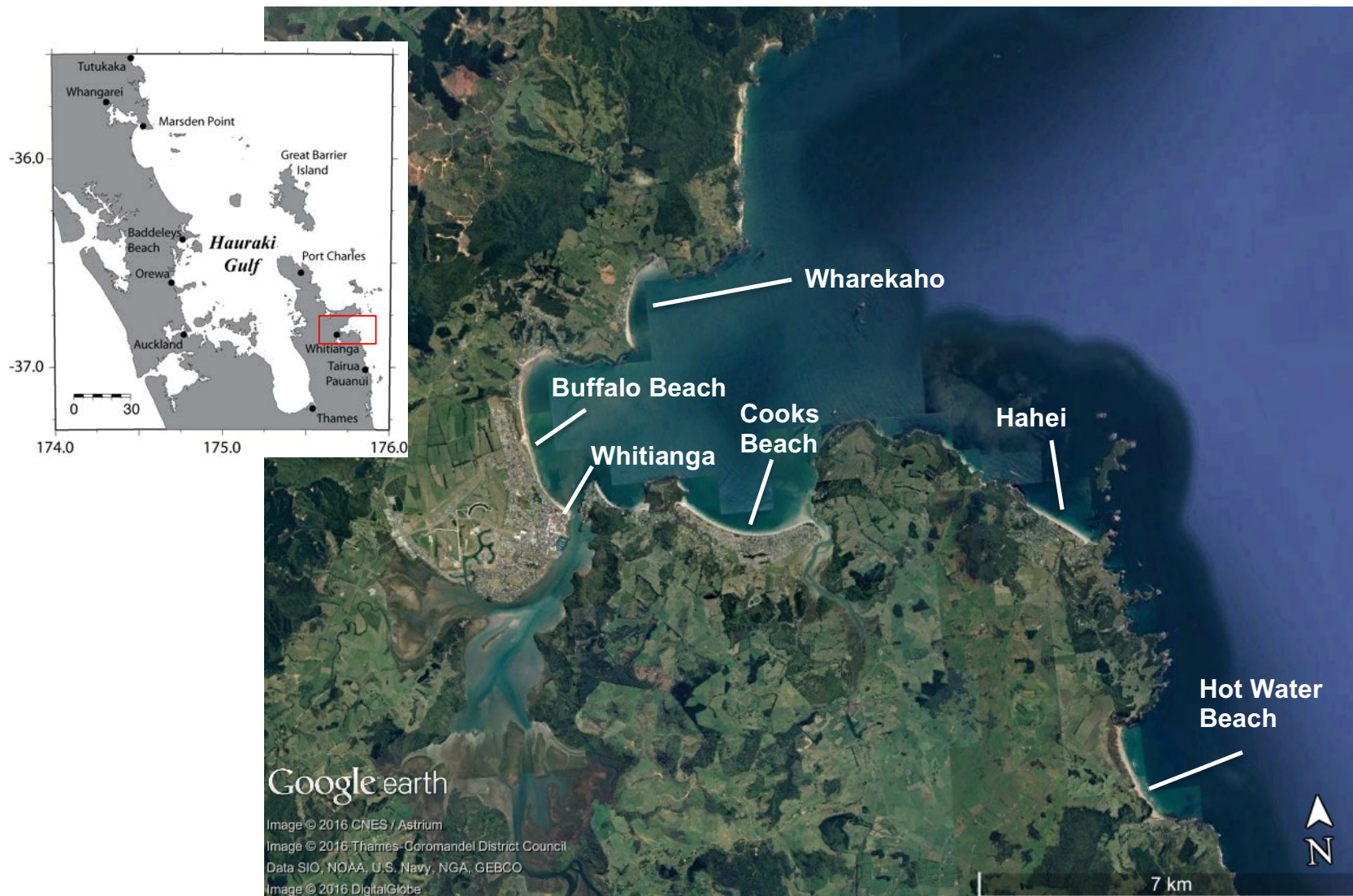


Figure 1.1 Location map for the study sites in and around Whitianga and Mercury Bay, New Zealand.

### 1.1 Review of Recent Literature

As noted above, this study extends the work of Prasetya et al. (2008) and provides inundation estimates for additional areas along the Coromandel Peninsula for both near source and distant source tsunamis.

Important results that came from the Prasetya et al. (2008) study include:

- Recognition of the importance of the source data for developing an accurate terrain model. They described the effect of terrain models derived from ground-striking and non-ground-striking LiDAR source data on tsunami inundation.
- Characterising the early onset hazard associated with Tonga-Kermadec trench sources.
- Assessing the relative severity of tsunami effects as it relates to the source mechanism and location.

Since the Work of Prasetya et al., (2008), an additional study by Prasetya and Wang (2011) investigated the recurrence of tectonic tsunami sources located along the Kermadec Trench and in the Bay of Plenty. Their analysis provides a suite of potentially tsunamigenic earthquake sources for the Kermadec Trench and is used as the basis for the modelling presented here.

The work presented here is built upon a series of recent reports produced by eCoast on behalf of the Waikato Regional Council (WRC) and the Thames Coromandel District Council (TCDC). The studies listed below all use a consistent methodology to quantify the tsunami hazard along the east coast of the Waikato region.

Borrero, J. C. (2013). *Numerical modelling of tsunami effects at two sites on the Coromandel Peninsula, New Zealand: Whitianga and Tairua-Pauanui*, (Waikato Regional Council Technical Report No. 2013/24, ISSN 2230-4363 (Online).

Morris, B. and Borrero, J. C. (2014) *Inundation of Whitianga town during the 1960 Chilean Tsunami*, Waikato Regional Council Technical Report 2014/65, June 2014, ISSN 2230-4363 (Online).

Borrero, J. C. (2014). *Numerical modelling of tsunami effects at Whangamata, Whiritoa and Onemana, Coromandel Peninsula New Zealand*, Report prepared for the Waikato Regional Council, September 2014.

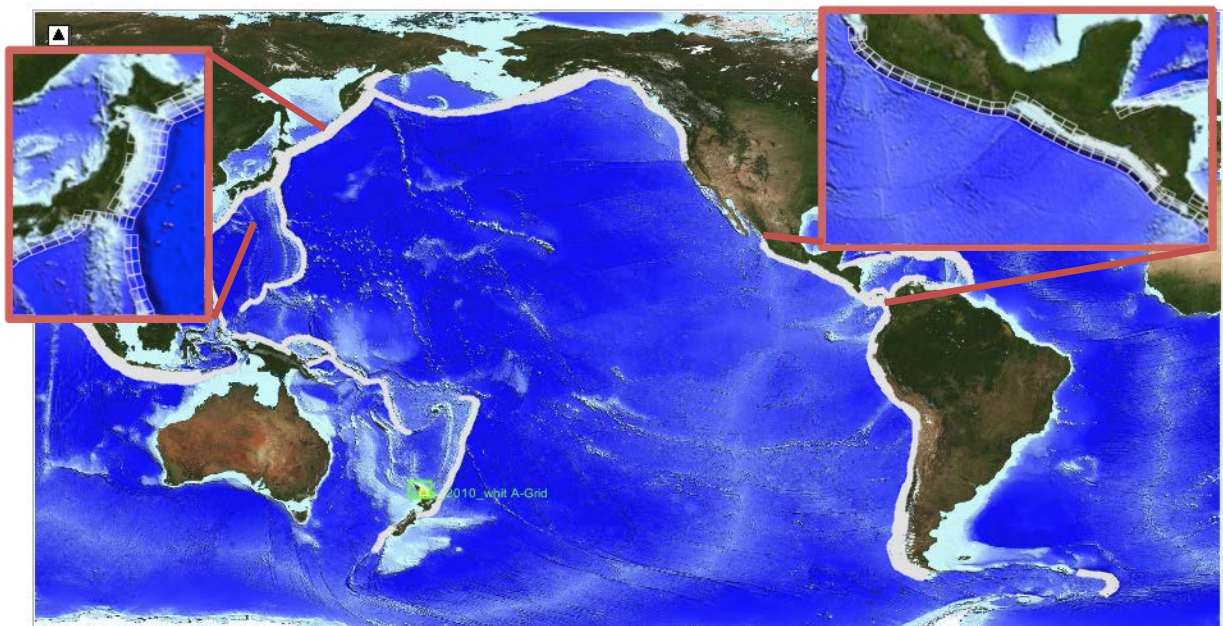
Borrero, J. C. (2015) *Numerical modelling of tsunami effects at Port Waikato, Raglan and Aotea Waikato West Coast, New Zealand*, Prepared for Waikato Regional Council, December 2015.

Borrero, J. C. (2015) *Numerical modelling of tsunami inundation along the Kennedy Bay to Opito Bay coast, Coromandel Peninsula, New Zealand*, Prepared for Waikato Regional Council, December 2015.

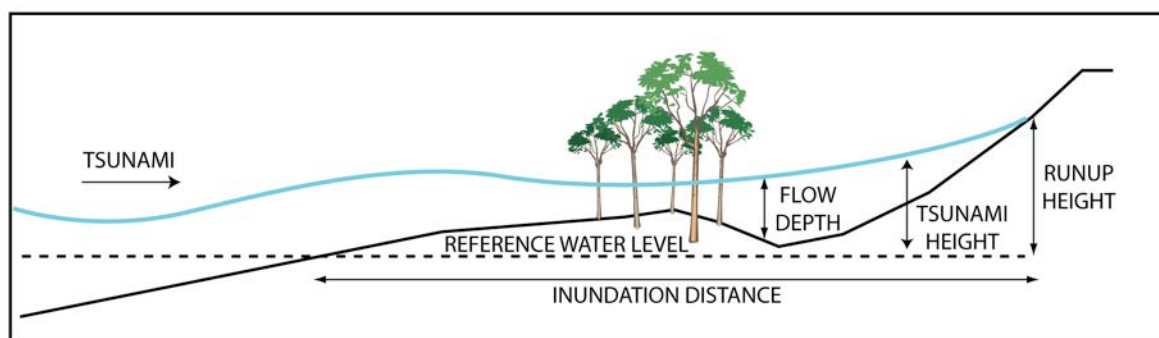
## 1.2 Modelling Approach

The numerical modelling presented in this study was carried out using the Community Model Interface for Tsunamis (ComMIT) numerical modelling tool. The ComMIT model interface was developed by the United States Government National Oceanic and Atmospheric Administration's (NOAA) Centre for Tsunami Research (NCTR) at the Pacific Marine Environmental Laboratory (PMEL) following the December 26, 2004 Indian Ocean tsunami as a way to efficiently distribute assessment capabilities amongst tsunami prone countries.

The backbone of the ComMIT system is a database of pre-computed deep water propagation results for tsunamis generated by unit displacements on fault plane segments (100 x 50 km) positioned along the world's subduction zones. Currently, there are 1,691 pre-computed unit source propagation model runs covering the world's oceans included in the propagation database. Using linear superposition, the deep ocean tsunami propagation results from more complex faulting scenarios can be created by scaling and/or combining the pre-computed propagation results from a number of unit sources (Titov et al., 2011). The resulting trans-oceanic tsunami propagation results are then used as boundary inputs for a series of nested near shore grids covering a coastline of interest. The nested model propagates the tsunami to shore computing wave height, velocity and overland inundation. The hydrodynamic calculations contained within ComMIT are based on the MOST (Method Of Splitting Tsunami) algorithm described in Titov and Synolakis (1995, 1997) and Titov and Gonzalez (1997). The ComMIT tool can also be used in conjunction with real time recordings of tsunami waveforms on one or more of the deep ocean tsunameter (DART) stations deployed throughout the oceans to fine tune details of an earthquake source mechanism in real time. An iterative algorithm that selects and scales the unit source segments is used until an acceptable fit to the observed DART data is met.



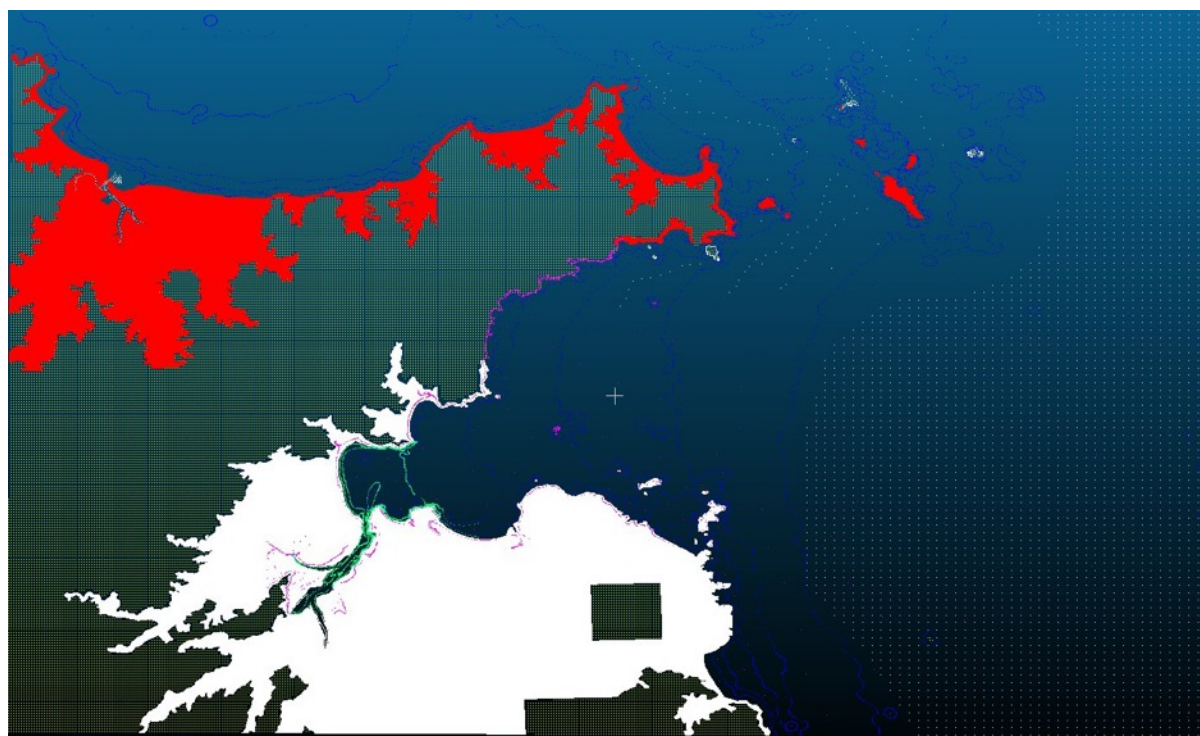
**Figure 1.2** The ComMIT propagation model database for tsunamis in the world's oceans. Insets show the details of the source zone discretization in to rectangular sub-faults.



**Figure 1.3 Definition sketch for tsunami height, flow depth, runup and inundation distance.**

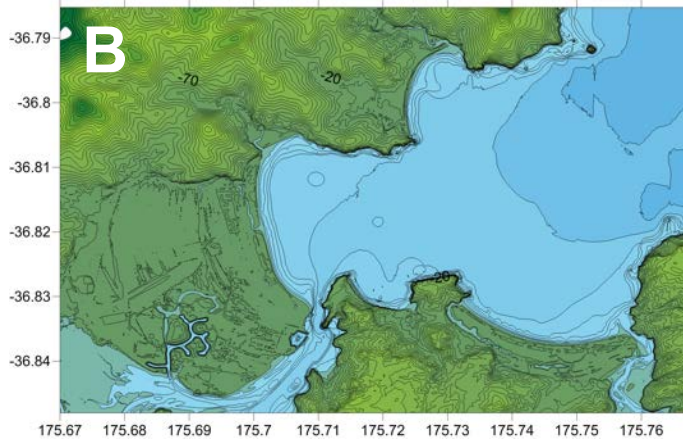
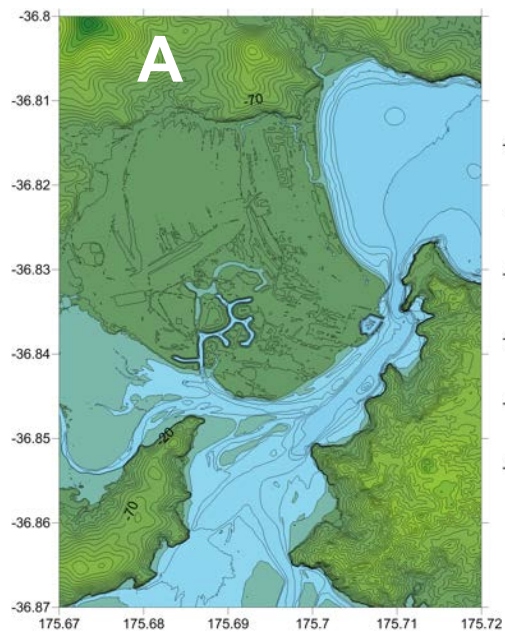
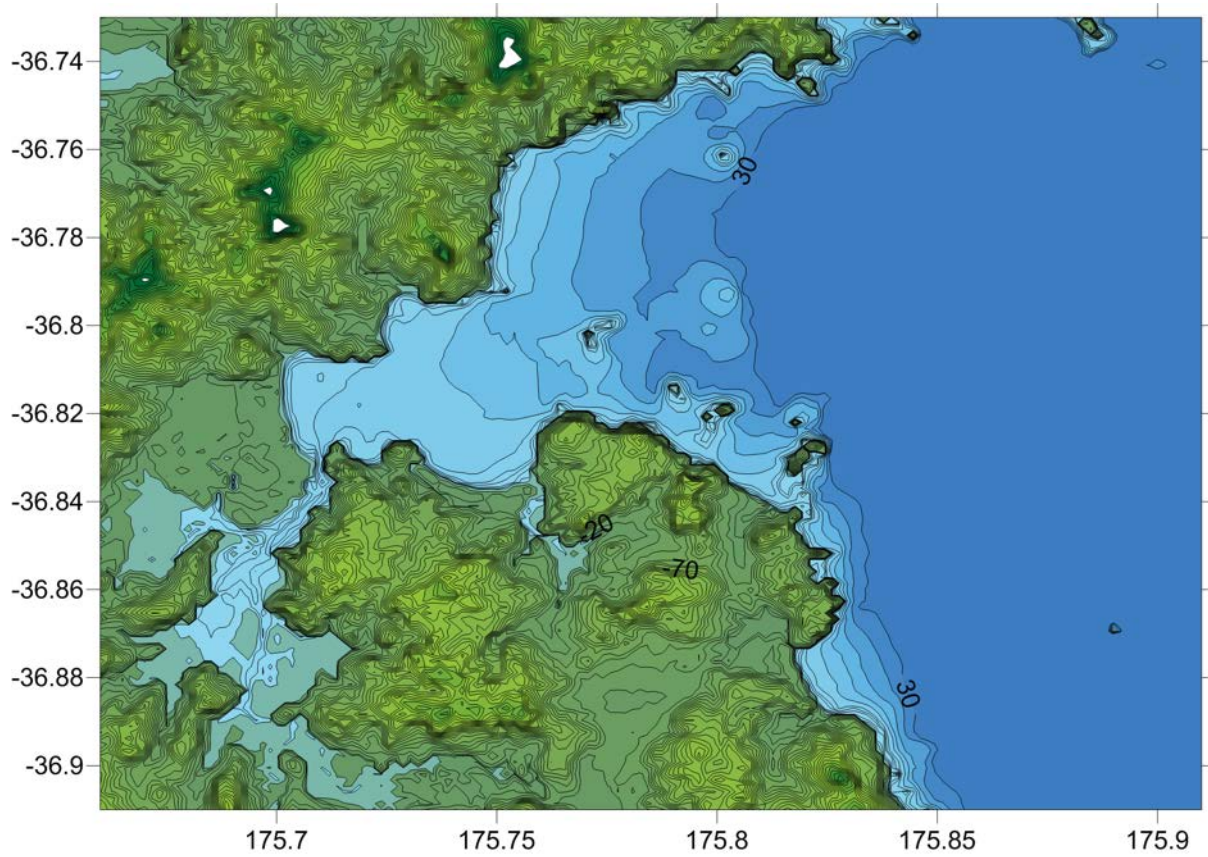
### **1.3 Numerical Modelling Grids**

The Waikato Regional Council provided raw bathymetry and LiDAR topography data for construction of the numerical modelling grids. The data were provided with a reference datum of MSL and a WGS84 projection. The data were combined with additional data sets covering the regional offshore bathymetry and on land topography. This included the Shuttle Radar Topography Mission (SRTM) 90 m resolution topography, 200 m resolution bathymetry from NIWA, as well as nautical chart data from Land Information New Zealand (LINZ). The coverage areas of the various data sets are shown in Figure 1.4. The data were combined in to a master set of (x, y, z) triplets and then gridded in to different resolutions and coverage areas using a Kriging algorithm (Figure 1.5). Model grids were set up for both mean sea level (MSL) and mean high tide (HT).



**Figure 1.4 coverage area of the different bathymetry data sets. Yellow: SRTM topography, Red and White: WRC supplied LiDAR, Aqua and Purple: LINZ digitised charts contours and sounding points.**





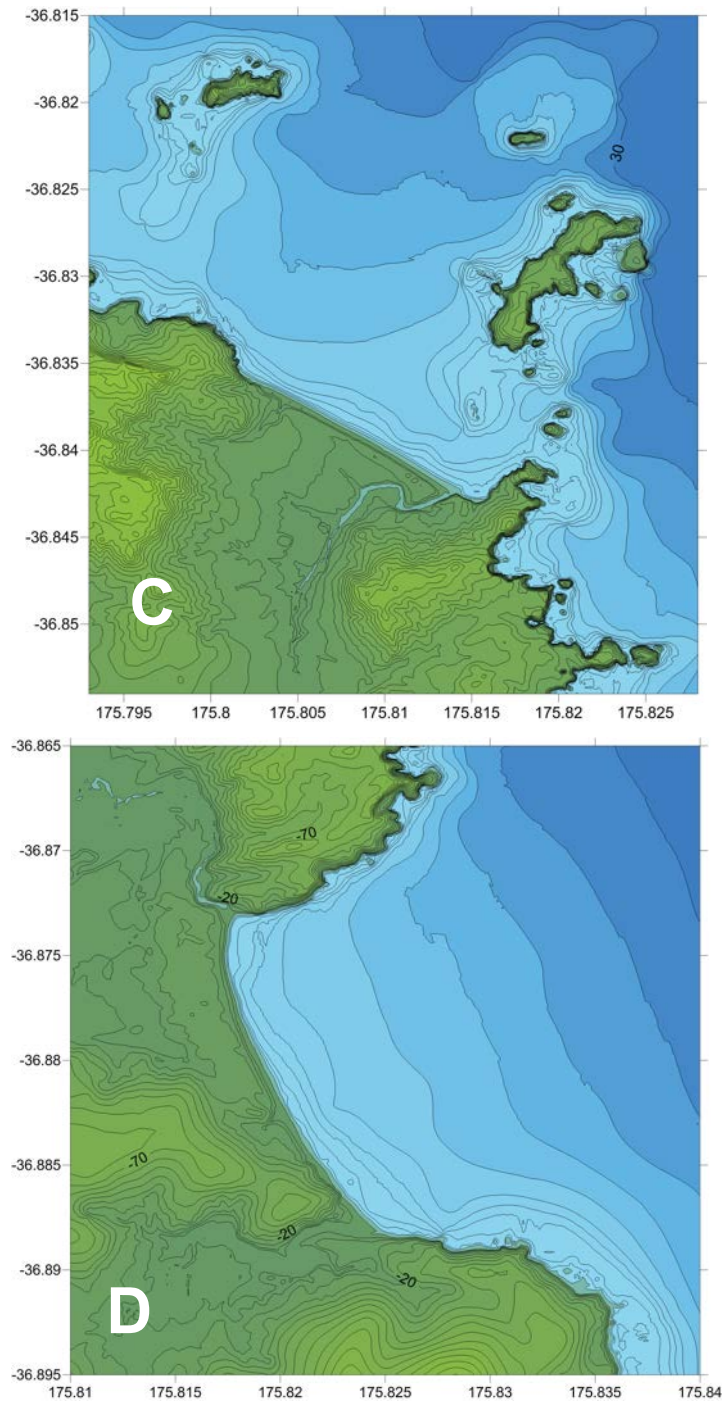


**Figure 1.5 The final numerical modelling grids: B grid (previous page top) at 150 m resolution. A) Buffalo Beach and the entrance to Whitianga Harbour B) An extended Buffalo Beach grid that include Cook’s Beach and Wharekaho C) Hahei and D) Hot Water Beach at 10 m resolution.**

## 2 TSUNAMI SOURCE MODELS

For this study we focused on tsunamis generated by both near source and distant source tectonic events. For the near source scenarios, we use a range of hypothetical earthquakes on the Tonga-Kermadec trench, which lies to the east of New Zealand. For the distant source scenarios we explore the effects of historical events including the 1960 Valdivia, Chile earthquake, the 2010 Maule Chile earthquake and the 1868 Arica Chile earthquake. An additional set of scenarios looks at the relative hazard posed by an earthquakes similar to the 1960 event positioned along the coast of Northern Chile and Peru, in a locations that may be more favourable for wave energy transmission towards New Zealand (Power and Gale 2011).

### 2.1 Near Source Tonga-Kermadec Trench Scenarios

The Kermadec trench scenarios are based on the work presented in Prasetya and Wang (2011) and Power et al., (2011). In that study they presented a number of potential source mechanisms based on an extensive literature review of the tectonics of the Kermadec Trench. For this analysis, we used eight different source models; two M8.9 earthquake sources with ~10.5 m average slip, two M9 earthquake sources with 14.9 m of average slip, two M9.1 sources with 20.9 m of average slip and two cases replicating the variable slip distribution of the 2011 Tohoku earthquake (responsible for the great Pacific tsunami of March 11, 2011). The sources are shown in Figure 2.1 through Figure 2.3 and described in Table 2.1. Each of the sources is positioned at two locations; one situated some 200 km north of East Cape and the other extending from the northern tip of East Cape. The TK 8 scenario is regarded as a maximum credible event from the Tauranga-Kermadec Trench source area.

**Table 2.1 Tsunami source models on the Tonga Kermadec Trench considered in this study.**

Number	Source
TK 1	M 8.9, 10.5 m uniform slip, 600x100 km fault plane, 200 km north of East Cape
TK 2	M 8.9, 10.5 m uniform slip, 600x100 km fault plane, 0 km north of East Cape
TK 3	M 9.0, 14.8 m uniform slip, 600x100 km fault plane, 200 km north of East Cape
TK 4	M 9.0, 14.8 m uniform slip, 600x100 km fault plane, 0 km north of East Cape
TK 5	M 9.1, 20.9 m uniform slip, 600x100 km fault plane, 200 km north of East Cape
TK 6	M 9.1, 20.9 m uniform slip, 600x100 km fault plane, 0 km north of East Cape
TK 7	M 8.8, Variable slip model, equivalent to 2011 Tohoku tsunami source positioned 200 km north of East Cape
TK 8	M 8.8, Variable slip model, equivalent to 2011 Tohoku tsunami source positioned 0 km north of East Cape

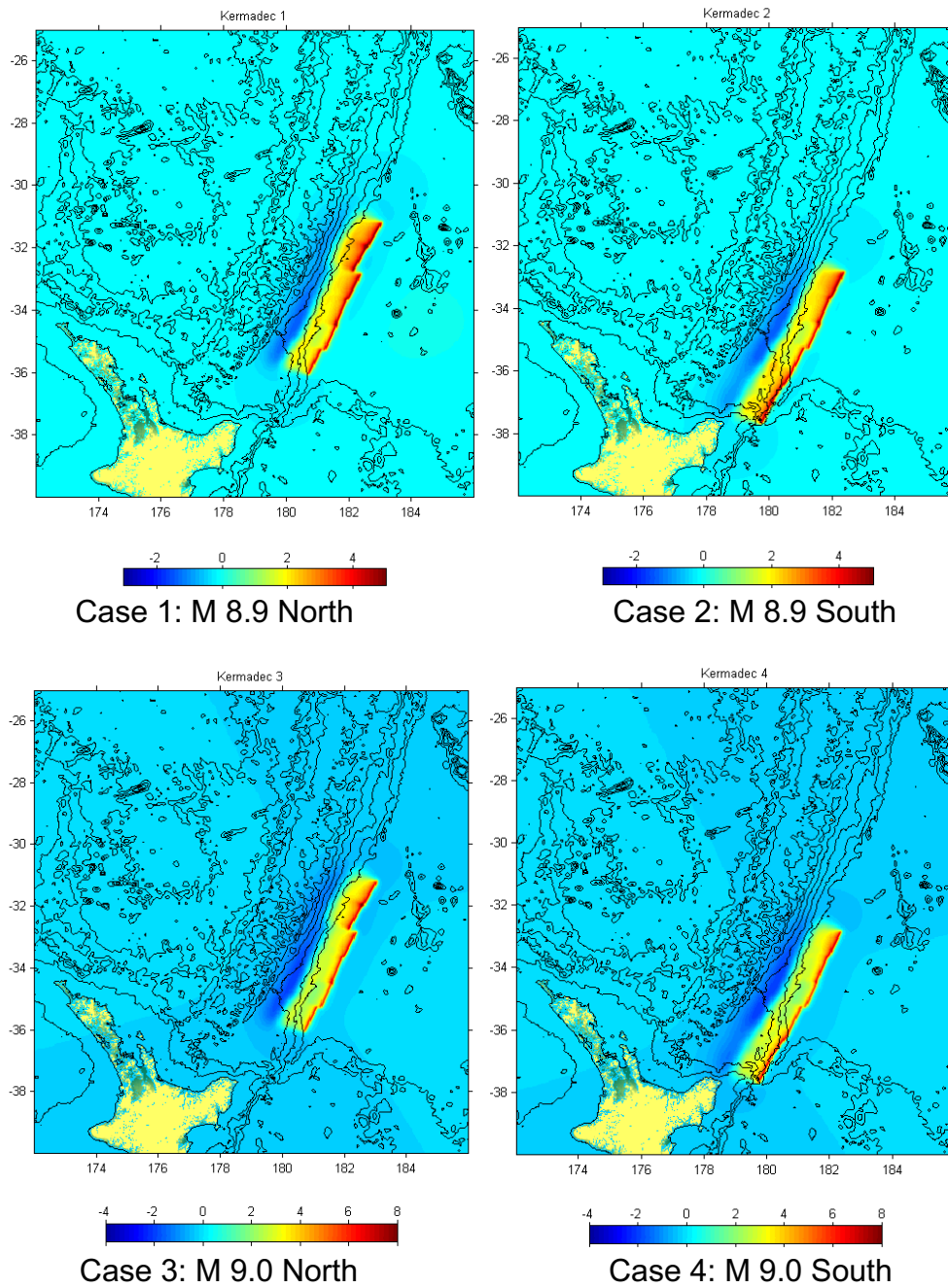


**Figure 2.1 Case 1, 2: 600 x 100 km fault 10.47 m average slip, M = 8.9. Case 3, 4: 600 x 100 km fault, 14.8 m average slip, M = 9. Note the change in the colour scale for cases 3 and 4.**

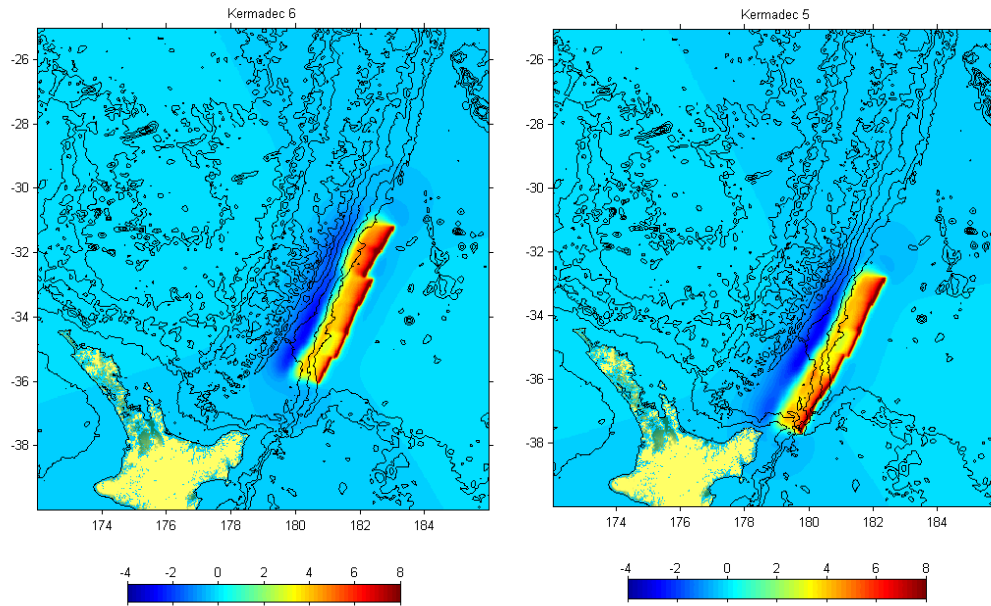


**Figure 2.2 Cases 5 and 6: 600 x 100 km fault, 20.9 m average slip,  $M = 9.1$**

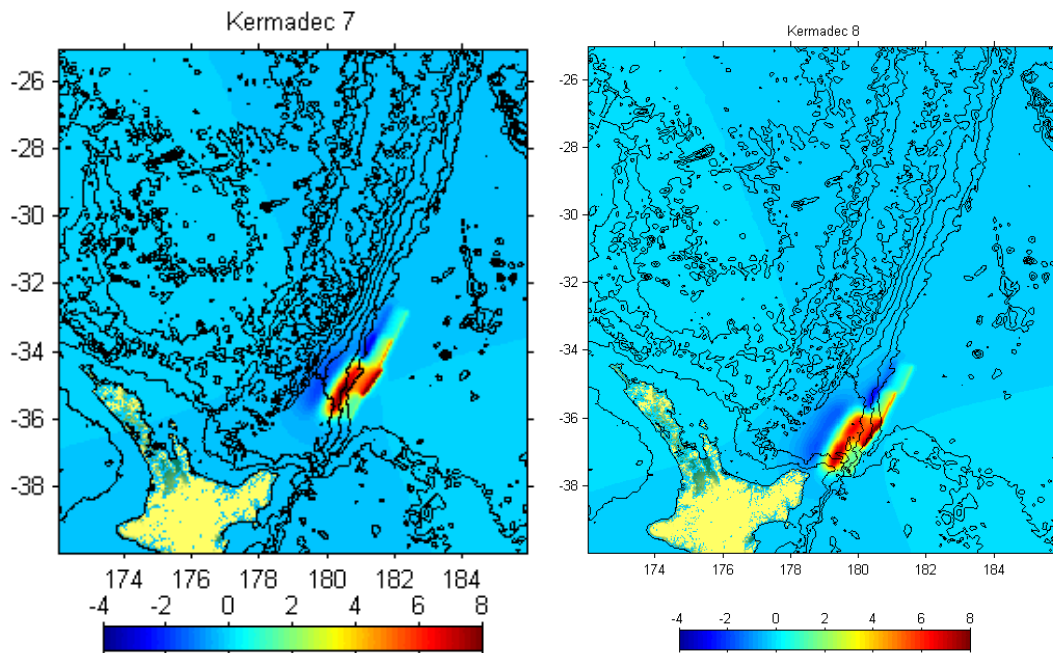


**Figure 2.3 Case 7 (left) the Japan 2011 tsunami source positioned 200 km north of the East Cape ( $M = 8.8$ ). Case 8 (right) the Japan 2011 tsunami source positioned at the southern end of the Tonga-Kermadec Trench ( $M = 8.8$ ).**

## 2.2 Distant Source Tsunami Models

In total, eight distant source events considered. Three are based on historical events (1868 Arica, 1960 Valdivia and 2010 Maule). Four additional sources are derived from the source model for the 1960 Valdivia earthquake but are positioned at different locations and with different slip distributions. An eighth scenario representing the 2011 Japan tsunami is presented for model validation purposes. The sources are listed in Table 2.2 and are described in the sections below. The FF 7 scenario is regarded as a maximum credible event for distant source tsunami.

**Table 2.2 Description of the distant source tsunami scenarios.**

Number	Source
FF 1 'Chile 1960'	The 1960 Valdivia, Chile earthquake. Source model based on Fujii and Satake (2012) (M ~9.2)
FF 2 'Chile 2010'	The 2010 Maule, Chile earthquake, source derived from NOAA real-time tsunameter inversion. (M ~8.8)
FF 3 'Arica 1868'	1868 Arica – A very large magnitude event (M ~9.4) extending from Arica, Chile 600 km northward into southern Peru. Source uses uniform slip of 39.6 m over the fault plane.
FF 4 'Chile North 1'	Chile North 1 – A variant of the Fuji and Satake (2012) source for the 1960 tsunami modified to concentrate largest amounts of slip towards the north of the fault rupture and positioned such that the deformation region runs from northern Chile towards the south. (M ~9.1)
FF 5 'Chile North 2'	Chile North 2– A variant of the Fuji and Satake (2012) source for the 1960 tsunami modified to concentrate largest amounts of slip towards the north of the fault rupture and positioned such that the deformation region straddles the Peru/Chile border with the largest deformation occurring offshore of southern Peru. (M ~9.2)
FF 6 'Chile North 3'	Chile North 3– A variant of the Fuji and Satake (2012) source for the 1960 tsunami modified to concentrate largest amounts of slip towards the south of the fault rupture and positioned such that the deformation region straddles the Peru/Chile border with the largest deformation occurring offshore of northern Chile. (M ~9.2)
FF 7 'Central Peru'	Peru – A variant of the Fuji and Satake (2012) source for the 1960 tsunami modified to concentrate largest amounts of slip towards the south of the fault rupture and positioned along the coast of Central Peru. (M ~9.2)
FF 8 'Japan 2011'	The 2011 Tohoku, Japan event. (M ~8.8)

### 2.3 Historical South American Tsunami Scenarios: 1960 Valdivia, 2010 Maule and 1868 Arica Earthquakes and Tsunamis

Two modern historical tsunami events are modelled in this study; the first is the 1960 Valdivia, Chile earthquake and the second is the 2010 Maule, Chile earthquake. Of the two, the 1960 event, which occurred in southern Chile, was much larger in terms of the earthquake magnitude and the tsunami height both in the near and far-field.

Borrero (2013) conducted a detailed analysis of the effects of the 1960 tsunami at Whitianga. In that study he compared the numerical model results from 6 different versions of the tsunami source for that event to eyewitness accounts and observations of inundation at Whitianga. The results of that study suggested that the earthquake slip distribution proposed by Fujii and Satake (2012) provided the best fit to the overall observed effects. However, it was necessary to increase the overall slip amounts by 20% to most accurately reproduce the observed inundation. The fault segments, initial seafloor deformation and slip amounts used for that source are shown in Figure 2.4 and Table 2.3.

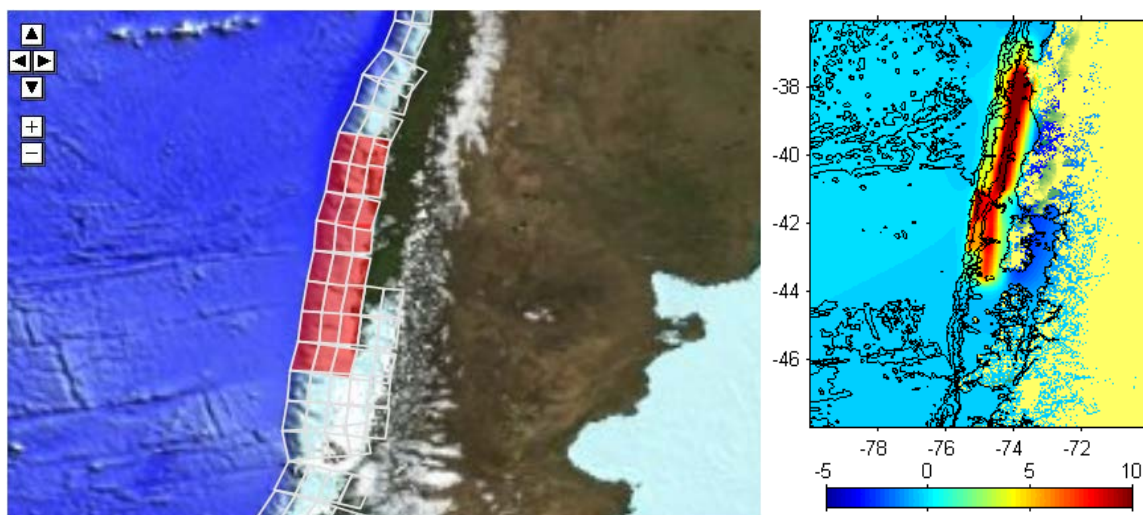
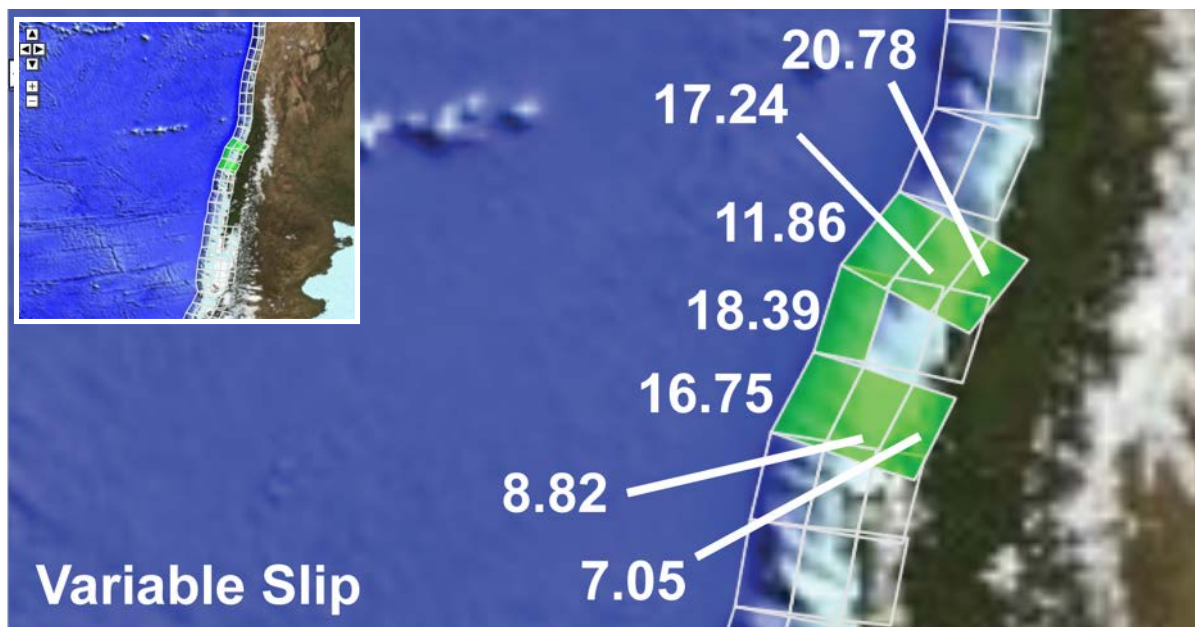


Figure 2.4 (left) Unit source segments used to define the 1960 Chilean Earthquake suite of events. (right) initial sea floor deformation at the source region.

Table 2.3 Faults segment slip amounts for the 1960 Chilean tsunami.

Fault Segment Slip Amounts		
5.0	12.9	1.2
6.6	36.1	21.0
2.8	31.1	11.3
4.9	29.6	11.5
7.8	32.9	6.6
25.7	17.8	6.2
15.3	21.7	5.5
3.7	20.5	2.7

On February 27, 2010 an earthquake with a moment magnitude ( $M_w$ ) of 8.8 (United States Geological Survey) occurred in the coastal area of southern Chile. The earthquake caused a destructive tsunami in Chile and a moderate tsunami that was observed throughout the Pacific Ocean. The tsunami was clearly evident along the Coromandel Peninsula and resulted in the closure of the Whitianga Marina for 2 days. The source mechanism used for this simulation (Figure 2.5) was determined through the inversion of DART tsunameter data (NOAA/PMEL, pers. comm.).



**Figure 2.5 Source segments and slip amounts used to model the 2010 Chile tsunami.**

The third historical tsunami event we consider is that of 13 August 1868. While there were no instrumental recordings of this tsunami, there are detailed accounts of the wave effects in New Zealand (de Lange and Healey, 1986). It is interesting to note that the effects on the North Island seem to be less severe than those on the South Island, with reported tsunami heights of 1-2 m at Mount Maunganui, Great Barrier Island and in the Tamaki Estuary. Even at Port Charles, the tsunami was only described as 'a high tide'. This is in contrast to the effects a Lyttelton Harbour near Christchurch, where the observations of Gibson (1868) suggested a peak to trough tsunami height of ~7.6 m (25 feet) for the first tsunami wave. To model this event, we based our tsunami source on the rupture length estimate of 600 km presented in Dorbath et al., (1990). Using fault segments extending from Arica northward (Figure 2.6) the model is initialized with a uniform slip amount of 39.6 m. Borrero and Goring (2015) showed that this amount of slip was necessary to replicate the observed 7 m water level change observed in Lyttelton Harbour as described by Gibson (1868).

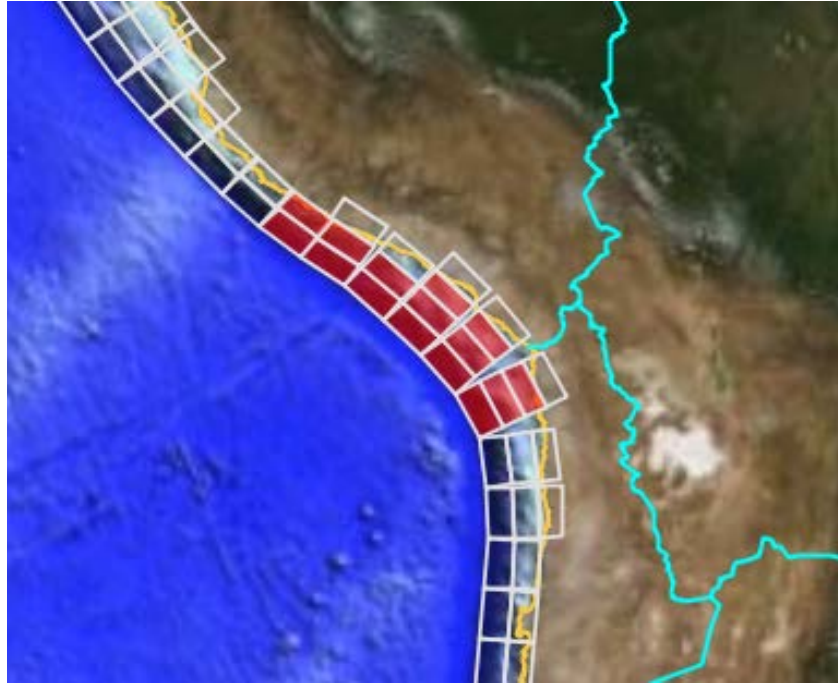


**Figure 2.6 Source segments used to model the 1868 Arica tsunami. A uniform slip amount of 39.6 m was applied to each segment.**

#### **2.4 Additional South American Tsunami Sources: Peru and Northern Chile**

Power et al. (2007) and Power and Gale (2012) showed that along the South American Subduction Zone, tsunamis generated along the Peru-Chile Border region have a greater impact along the New Zealand coast relative to sources located further to the north or south. Indeed, the 1960 event would have been more damaging in New Zealand had it occurred a few thousand km to the north. Furthermore the 1868 event generated run-up of 1 – 4 m in New Zealand (up to 10 m in the Chatham Islands) and resulted in New Zealand's only tsunami related fatality since European settlement. The event caused damage to boats and infrastructure along the east coast of the North and South Islands. This event was followed 11 years later by another earthquake of similar magnitude (~M8.8) located further south along the northern coast of Chile. This event however was not as damaging or well observed in New Zealand as the 1868 event. For this reason we felt it was prudent to explore the effects of such an event. The source models we used were based on source model for the 1960 Chilean earthquake described by Fujii and Satake (2012). However, Borrero (2013), showed that the Fujii and Satake slip amounts should be increased by 20% to match the inundation observed in Whitianga. He also showed that by aggregating the high slip regions together, the resultant tsunami in New Zealand was larger. Therefore, to better represent a maximum credible event, this study uses the higher slip amounts with the high slip areas clustered together. These source models were then positioned at different locations along the South American Subduction Zone to assess the impacts at the study sites.

We first start with scenarios positioned near the Peru-Chile border. For Distant Source 4 (FF4), we first position the Fujii and Satake (2012) source model towards the north of Chile. This source has the high slip regions clustered to the north of the earthquake rupture area. For source FF5, this same deformation pattern is shifted 600 km to the north. For source FF6, we use the same segments as FF5 and

reverse the deformation pattern to concentrate the slip to the south. The initial sea floor deformations used to initialize the hydrodynamic model are shown in Figure 2.8. The final distant source (FF7) is identical to FF6 with the entire deformation pattern shifted approximately 800 km north along the coast and situated off the coast of central Peru. This source also concentrates the high slip region to the south of the rupture area.

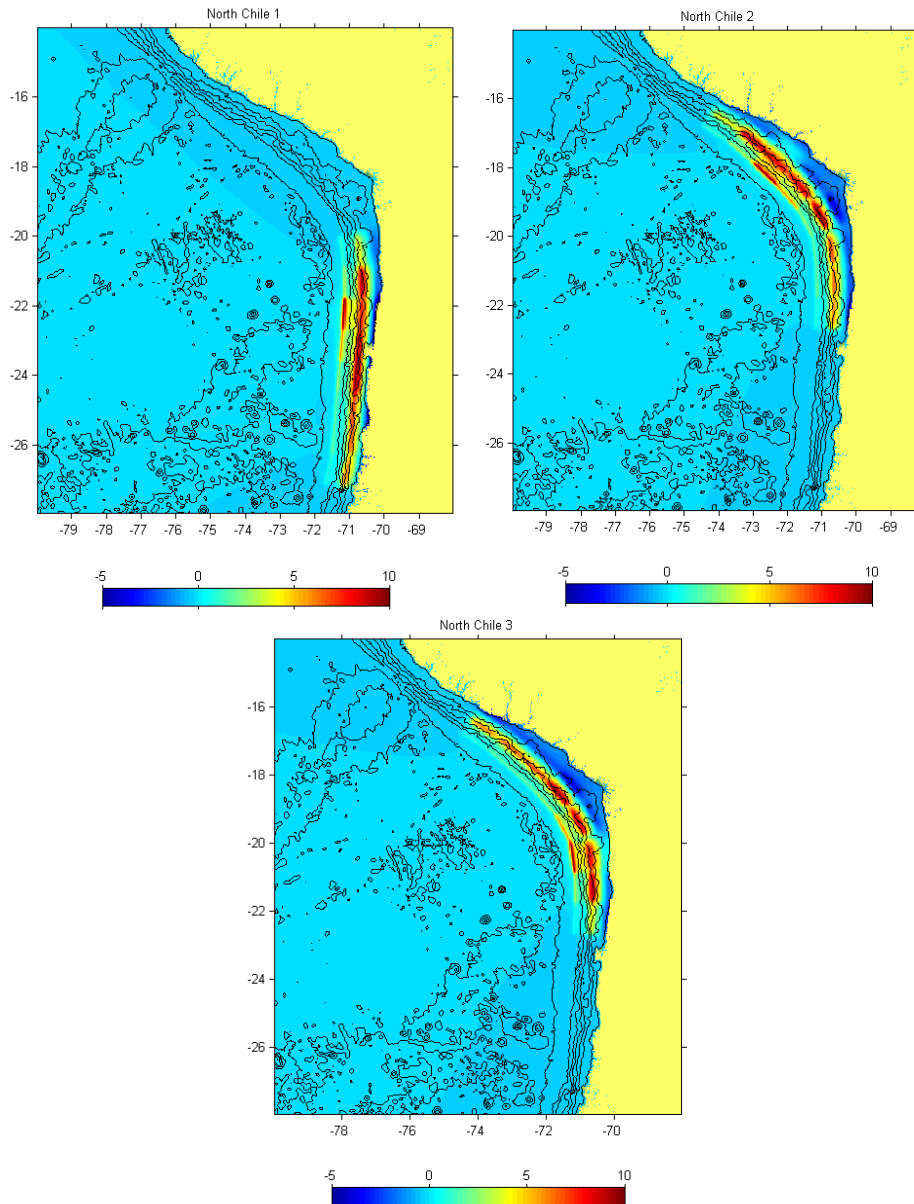


**Figure 2.7 Three additional South American sources. Variants of the Fujii and Satake (2012) source for the 1960 Chile earthquake are positioned along the coast of Northern Chile and Southern Peru.**

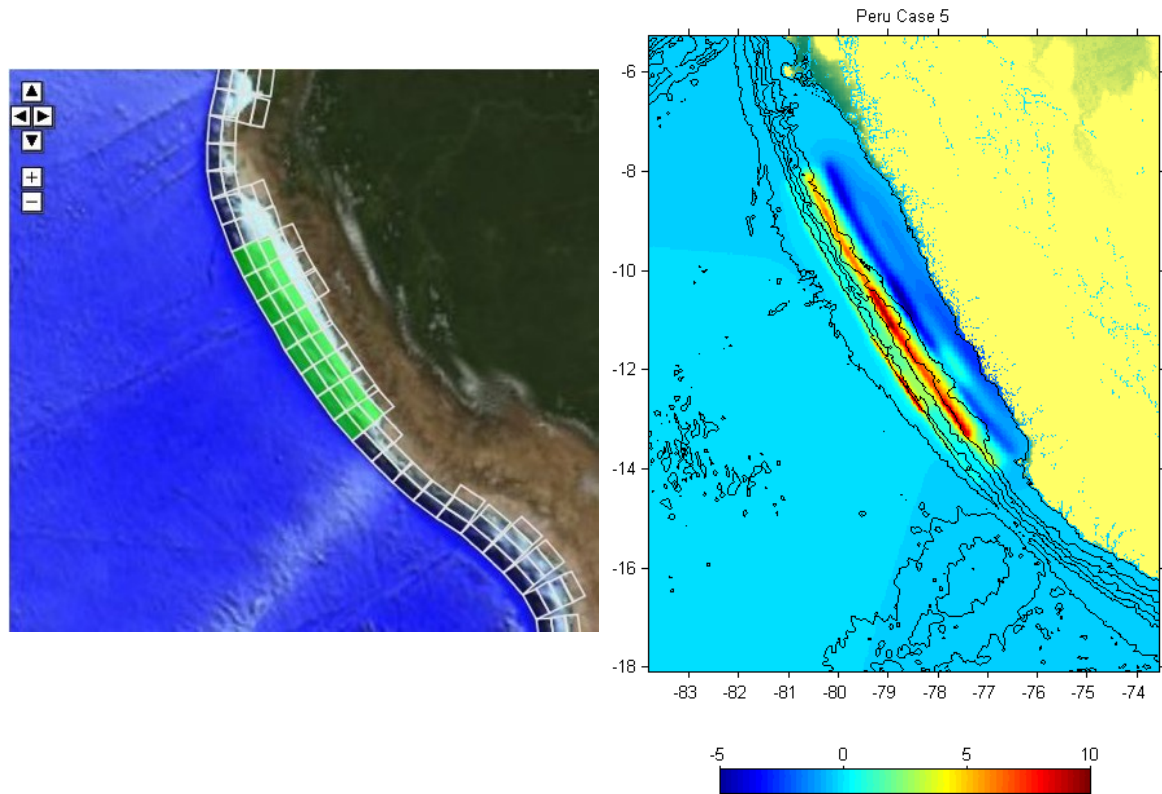


**Figure 2.8** Fault segments used to construct the Central Peru tsunami source (left) and the initial deformation field used to initialise the tsunami model (right).

### **2.5 The 2011 Tohoku, Japan Earthquake and Tsunami**

The model was also compared against tide gauge data recorded in Whitianga during the tsunami generated by the Great Tohoku earthquake which occurred on March 11, 2011. While several source models exist for the Tohoku earthquake, for this study we adopted the source determined through the direct inversion of measured tsunami wave forms on DART tsunameter stations located near the earthquake source region (Figure 2.9). This source mechanism was first made available to the global tsunami modelling community just hours after the earthquake and has been used extensively for model assessments in both the near and far-field (Borrero et al., 2012, Wei et al., 2012).

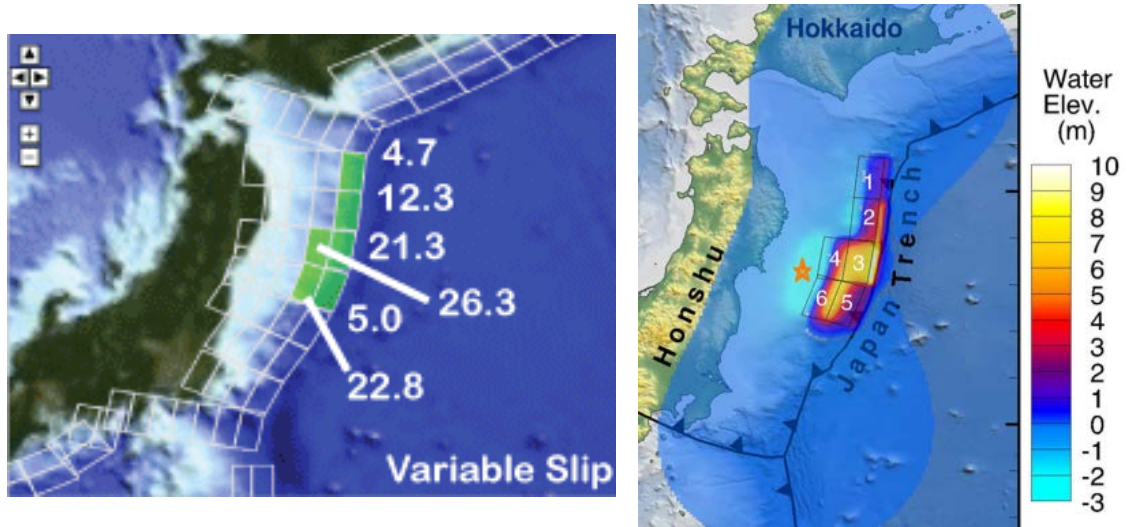


Figure 2.9 Source model used for the 2011 Tohoku tsunami, The amount of slip on each segment is indicated in the left panel, while the vertical deformation of the sea floor is shown on the right (image reproduced from Wei et al., 2012).

### 3 MODEL VALIDATION TO HISTORICAL EVENTS

Two records of tide gauge data from Whitianga are available from recent trans-Pacific tsunami events. These records provide the best available data sources for numerical model validation. Additionally, the 1960 Valdivia Chile tsunami caused inundation and damage in Whitianga and was widely observed and well documented.

#### 3.1 1960 Chile Tsunami

The effects of the 1960 tsunami in Whitianga were described in detail in Borrero (2012) and Morris and Borrero (2013). The modelling presented in those reports described a process of testing several different tsunami source models and analysing the results in terms of how well they matched the available observational records from that event. Ultimately a tsunami source model based on the earthquake slip distribution proposed by Fujii and Satake (2012) was shown to give the best fit to the majority of the available data. It is important to note that the strongest effects in Whitianga were observed more than seven hours after the tsunami arrival.

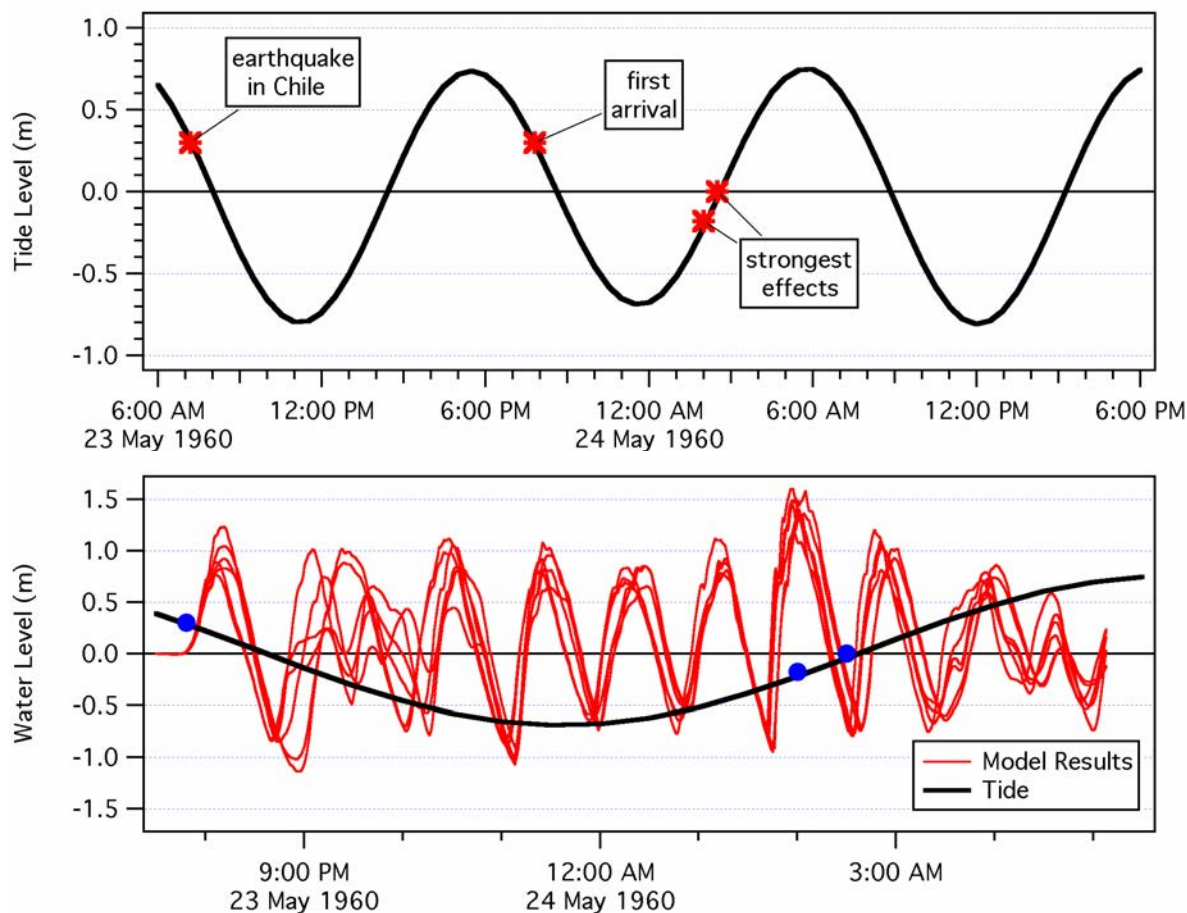


**Figure 3.1 (top)** The predicted tide on the day the 1960 Chile tsunami affected Whitianga. Important times are marked and noted. **(bottom)** Model results (red) for six source models compared to the predicted tide level (black). Blue dots indicate the modelled arrival time and the time when the worst effects were observed by the witnesses.

In this study we used that same source on the newer bathymetry and topography grids developed for the updated modelling presented here. The inundation results along Buffalo Beach for the 1960 event at mid and high tide are presented in Figure 3.2 and Figure 3.3. For the mid tide scenario, the model results seem to slightly under-predict the inundation extents whereas they may slightly over-predict in the high tide scenario. In reality, at the time of the 1960 event, the peak inundation extents occurred just at or below mid tide (see Figure 3.1).

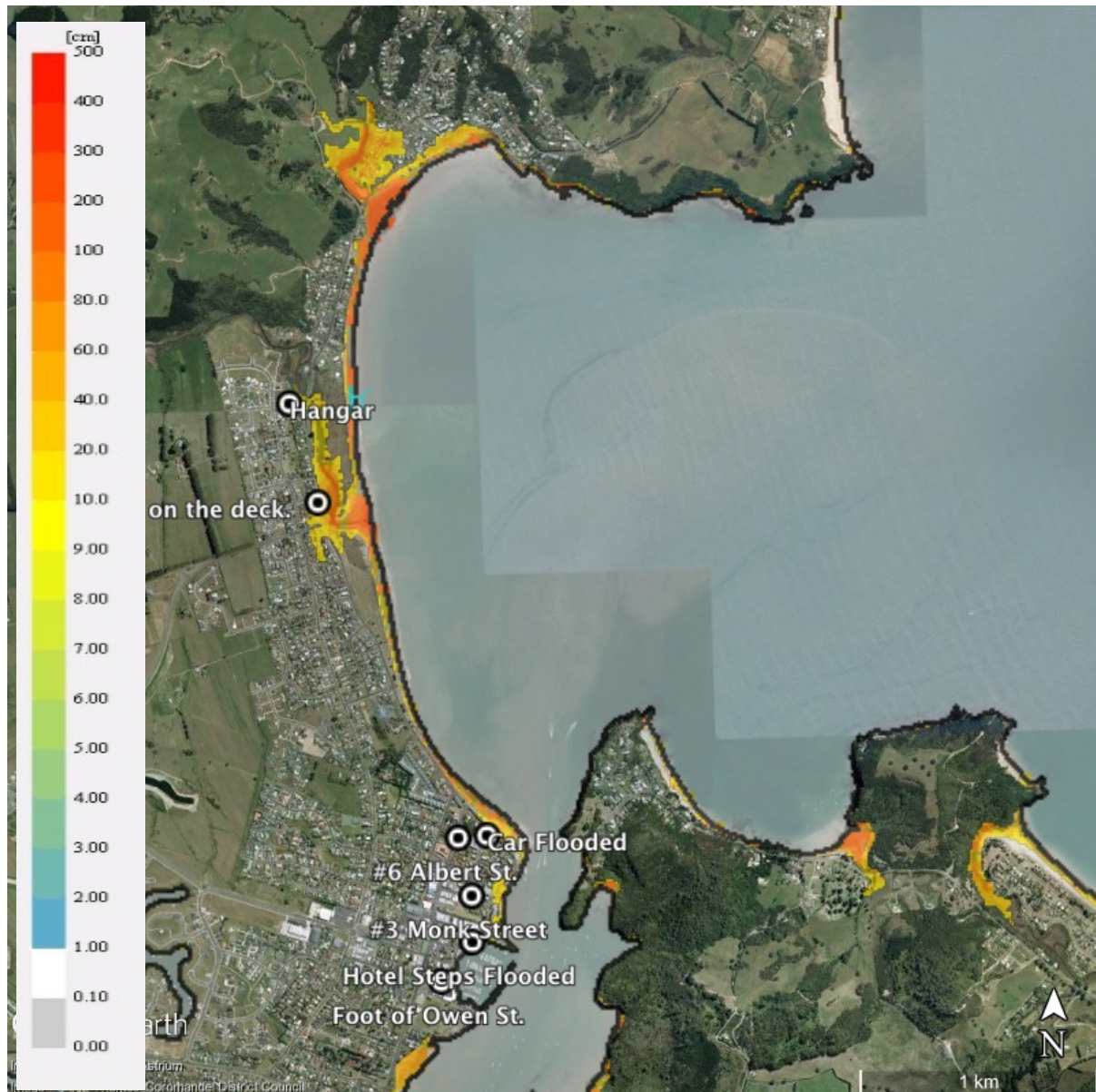


**Figure 3.2 Modelled inundation for the 1960 Chilean event assuming mid tide conditions. Locations noted on the map are places where inundation effects were recorded in 1960.**

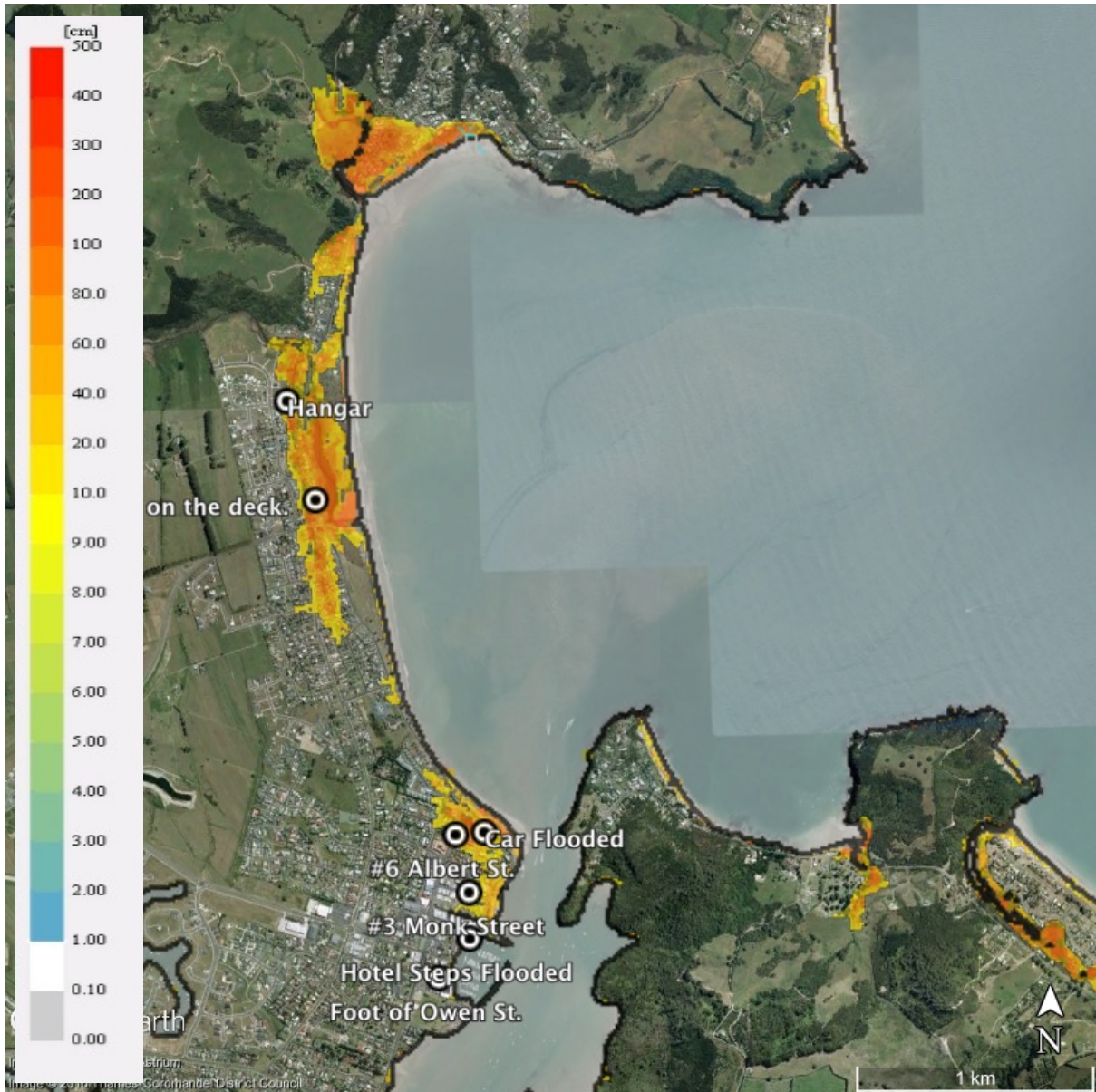


**Figure 3.3 Modelled inundation for the 1960 Chilean event assuming high tide conditions. Locations noted on the map are places where inundation effects were recorded in 1960.**

### 3.2 The Tsunamis of 2010 and 2011

The 27 February 2010 Chile earthquake occurred along South American Subduction Zone (SASZ), which is known to generate great earthquakes and transoceanic tsunamis. This event, the largest from the SASZ in half a century, originated some 230 km north of the source for the 1960 event. While the 2010 event was a big earthquake, it nucleated relatively deep on the subduction zone, causing the bulk of the energy release (20 m slip at 30 km depth) to occur at depth and minimizing its tsunami generation potential. Nevertheless the earthquake produced a locally devastating tsunami with runup heights approaching 30 m near Constitución in Southern Chile. In contrast, the 11 March 2011 Tohoku, Japan earthquake released nearly twice the energy of the Chilean earthquake, resulting in nearly 30 m of co-seismic slip at 20 km depth and rupture extending to the trench axis resulting in tsunami runup of over 40 m in the near field.

Both tsunamis were well recorded on tide gauges throughout New Zealand. Borrero and Greer (2013) studied in detail the characteristics of these tsunami events based on the available tide gauge data. Summary statistics of these tsunami on the Whitianga tide gauge are presented in Table 3.1. It is interesting to note that despite occurring on opposite sides of the Pacific Ocean, both tsunami reached Whitianga in approximately the same amount of time (~13 -14 hrs). Overall the 2011 tsunami produced slightly larger wave heights at Whitianga, however we must recall that the 2011 Japan earthquake was nearly twice as powerful as the 2011 Chile event. That the Japan tsunami was not much larger in New Zealand, or in Whitianga in particular is due primarily to the fact that New Zealand lies well south and off axis from the main beam of tsunami energy that emanated from the 2011 source area. It is also important to note that the strongest effects from both of these tsunami occurred several hours after the tsunami arrived. In the Chile event, the largest positive tsunami surge occurred 2.23 hours after arrival while the largest individual tsunami wave occurred just under 5 hours after arrival with the highest sea level during the event (tsunami plus tide) not occurring until nearly 1 full day after tsunami arrival. In the case of the Japan event, each of these three effects (maximum positive surge, largest total wave height and highest overall sea level) all occurred 4.6 hours after tsunami arrival. Based on eyewitness accounts, the strongest surges and most dangerous conditions occurred some 5-7 hours after the observed tsunami arrival time.

**Table 3.1 Summary statistics for the Japan and Chile tsunamis on the Whitianga tide gauge. The arrival time is in hours after the earthquake. P2T = Peak to Trough. The timing of the maximum tsunami heights, maximum wave cycle and maximum sea levels are given in hours relative to tsunami arrival time. Data from Borrero and Greer (2013).**

	Arrival Time	Max. amp. (m)	Assoc. Trough (m)	Max Height (m)	Hours after arrival	Max P2T (m)	Hours after arrival	Max SL (m)	Hours After Arrival
Chile	13.34	0.59	-0.45	1.04	2.23	1.23	4.99	1.18	23.56
Japan	13.04	0.78	-0.85	1.63	4.64	1.63	4.64	1.28	4.64

In Figure 3.4 and Figure 3.5 we plot the filtered (tide removed) time series of the measured tsunami water levels for the 2010 and 2011 tsunamis. Each plot also shows the wavelet spectrograms of the tsunami signal. The spectrograms show the relative strength of different spectral components of the tsunami signal. The spectrogram from the 2010 event shows an initial burst of energy starting early in the record and lasting for some 10 hours. This is followed by a secondary surge in energy starting approximately 4 hours later and lasting for approximately 6 hours.

The spectral signature of the 2011 Japan event is somewhat different with the energy arriving less abruptly and peaking some four hours after arrival. The record also shows an overall longer duration of a strong tsunami signal. The increase in energy seen 40-50 hours after the earthquake could possibly be the result of tsunami waves reaching New Zealand after reflecting off the west coast of South America.

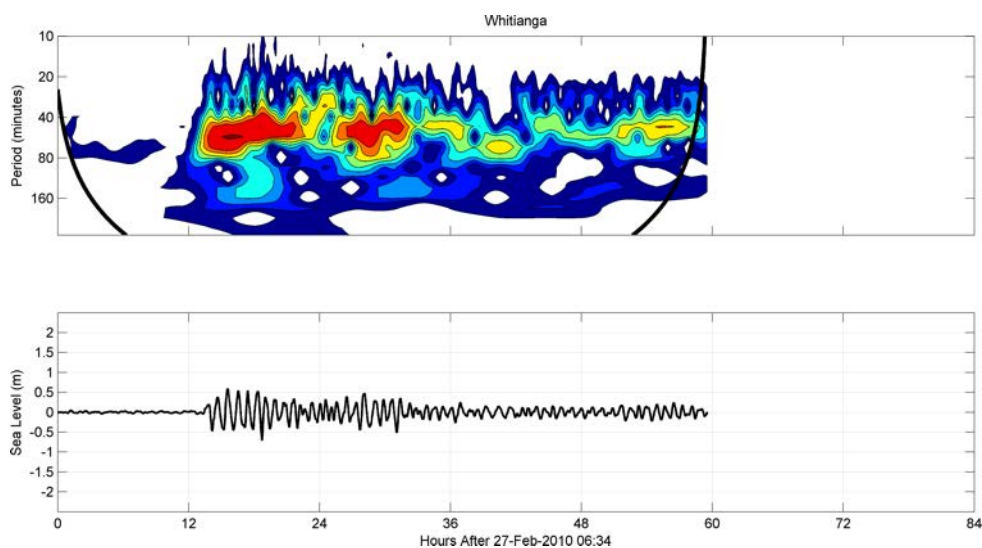


**Figure 3.4** Filtered tide gauge record of the 2010 Chile tsunami in Whitianga (bottom). Top plot shows the spectral content of the tsunami signal.

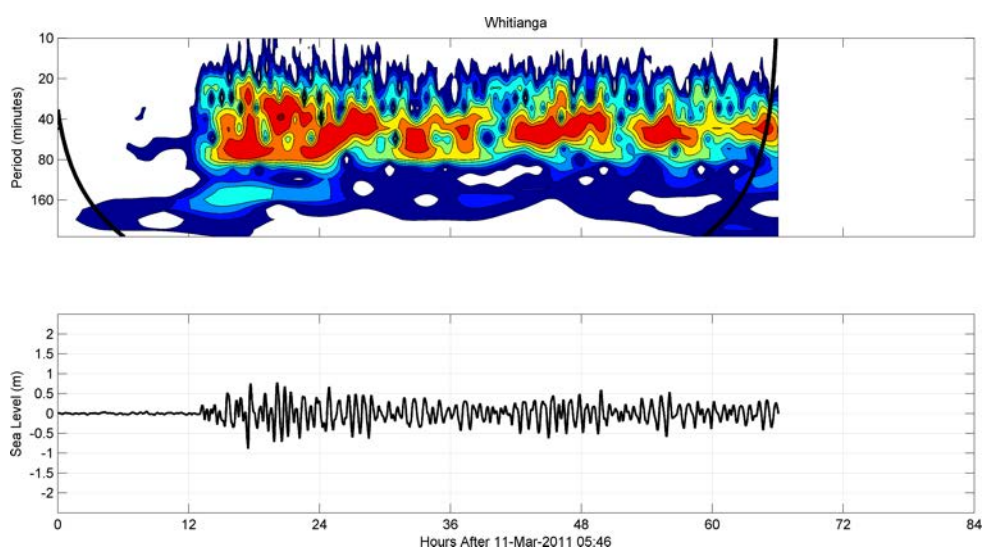


**Figure 3.5** Filtered tide gauge record of the 2010 Chile tsunami in Whitianga (bottom). Top plot shows the spectral content of the tsunami signal.

Below we present model result for the 2010 Maule Chile and 2011 Tohoku Japan tsunamis. The source models used for each of these simulation is presented in Section 2 above. Starting with the 2010 event, the model provides a good fit to the measured data. The arrival time is accurate and the first 3.5 wave cycles (over nearly 5 hours) are well represented in terms of tsunami amplitude and period. There is a noticeable over-prediction of the negative phase of the third wave cycle, however the subsequent wave peak matches the measured data well. Following this the model under-predicts two consecutive wave cycles and begins to fall out of phase with the measured data. This is then followed by several hours where the modelled tsunami matches the measured data in terms of wave amplitudes, but is out of phase with the tide gauge record. Despite this, the model predicts very well the critical factors such as the overall tsunami heights and the duration of the tsunami signal, including the larger wave heights seen some 15 hours after the tsunami arrival.

For the 2011 Japan tsunami (Figure 3.7) the model provides a good fit to the data in terms of tsunami arrival time and for the tsunami amplitudes over the first 6-7 hours of tsunami activity. Particularly notable is the high peak that is seen in the data and reproduced in the model results (albeit somewhat over-predicted) occurring approximately 17.5 hrs after the earthquake. After 7 hours of tsunami activity (approximately 20 hours after the earthquake) the model consistently under-predicts the measured tsunami heights. As noted above, this could be attributable to the fact that New Zealand lies well off axis from the main beam of tsunami energy and compounded by the fact that the tsunami must travel through the islands of the southwest Pacific. The complex, irregular bathymetry of these islands is not well represented in the global propagation model and may therefore lead to errors in the model output. Additionally, the source model used for this scenario was derived from records of the tsunami at DART tsunameters located very close to the source region. Inverting the source mechanism from other tsunameters located further afield could result in more accurate results in New Zealand. Despite these caveats, we maintain that the ability of the model to accurately predict the tsunami arrival and the first 6 hours of tsunami activity is a good result given the uncertainties inherent to the tsunami modelling process.

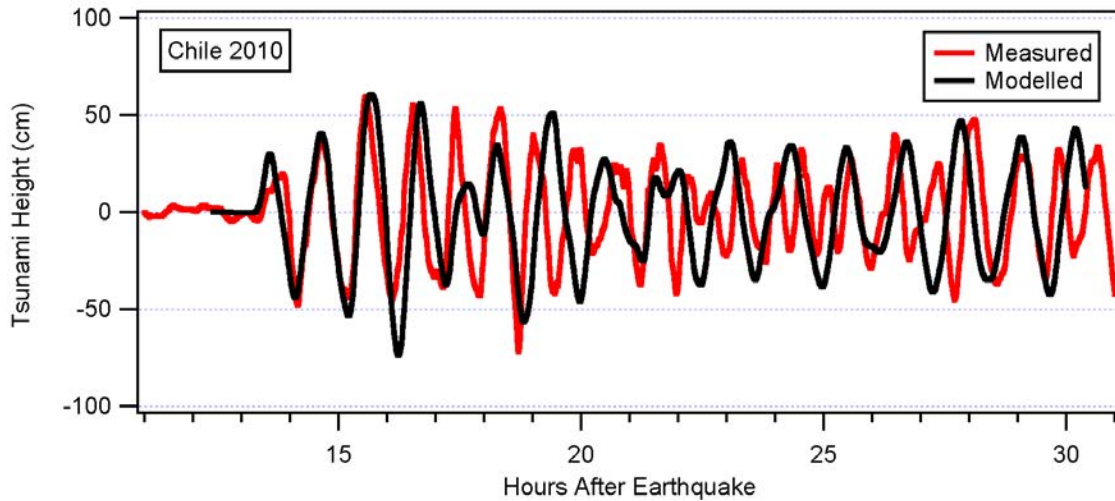


**Figure 3.6 Comparison of modelled to measured tsunami water levels at Whitianga from the 2010 Maule Chile tsunami.**

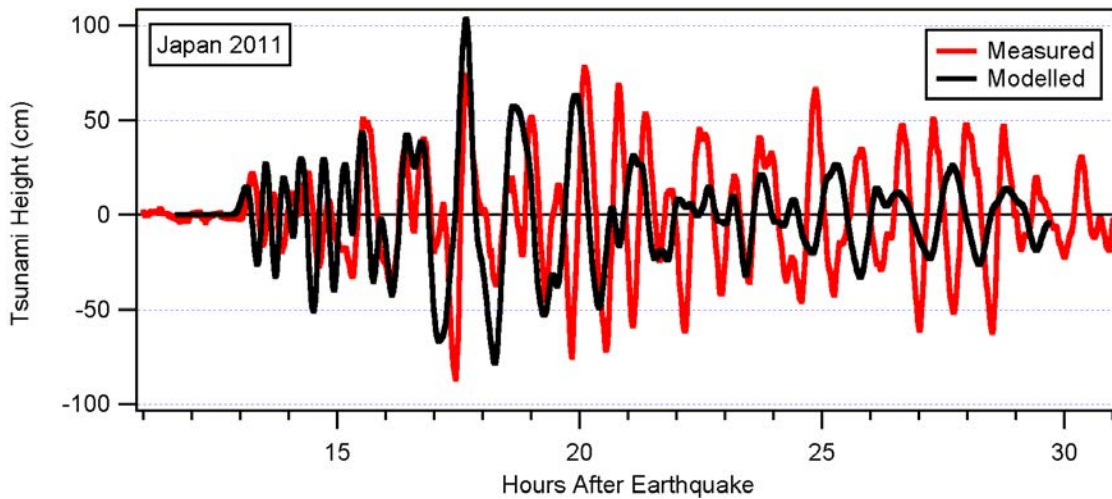


**Figure 3.7 Comparison of modelled to measured tsunami water levels at Whitianga from the 2010 Maule Chile tsunami.**

## 4 MODEL RESULTS: TONGA-KERMADEC TRENCH SOURCES

### 4.1 *Arrival Times*

An important consideration for the near source tsunami hazard is a clear understanding of the tsunami arrival time. ‘Tsunami arrival’ however can be defined in a number of ways whether it is the time of the first water motions (rise or drop) or the time of the maximum wave height. In Figure 4.1 we plot time series of modelled water level from each of the 8 TK scenarios. In these plots we see that the first withdrawal of the water surface begins approximately 1 hour after the earthquake for the even-numbered sources (1,3,5,7) and slightly earlier for the even numbered sources (2,4,6,8). Recall that the odd numbered sources are located slightly further north along the TK trench and thus more time is required for the wave to reach the shores of Mercury Bay. In each case the initial water level withdrawal is followed by the largest positive surge on the first wave, which peaks at 1.25 to 1.5 hours after the earthquake. A complete set of model output plots is presented in Appendix 1.

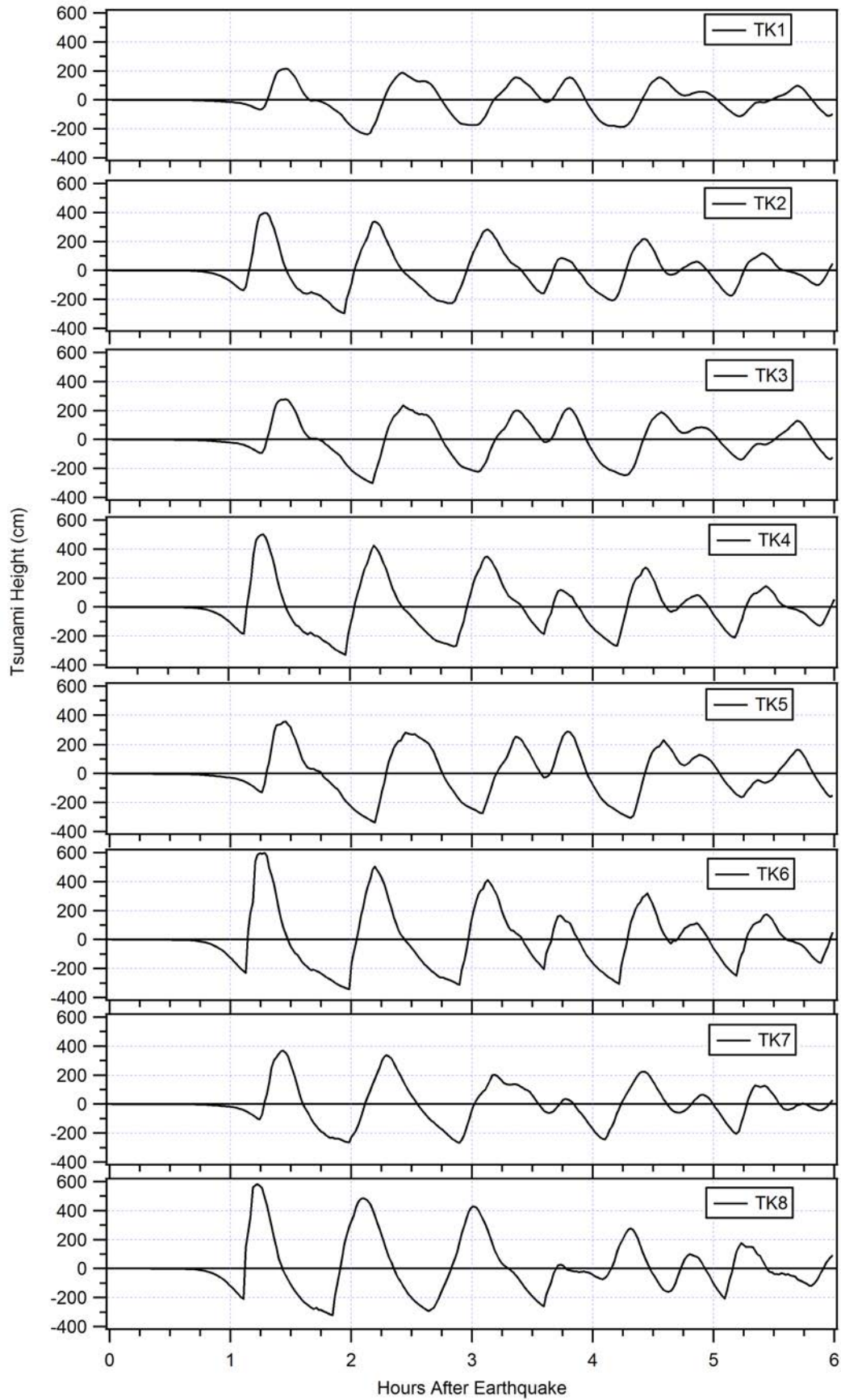


Figure 4.1 Water level time series plots for the 8 sources just off shore of Buffalo Beach.

## 4.2 Tsunami Height

For each of the tsunami source models, we simulated the tsunami inundation and current speeds for cases at mean sea level (MSL) and High Tide (HT). The most obvious difference in the model results at the study sites however was a result of the location of the seafloor deformation. For the sources located further south (even numbered sources 2,4,6,8), the tsunami induced wave heights were larger than for the equivalent sources shifted 200 km northward. This effect was illustrated in Borrero (2013) by showing the wave height produced offshore of the Coromandel Peninsula by identical tsunami generated on 11 different fault segments running from the East Cape northward along the TK Trench. The results (reproduced in Figure 4.2) show that the wave height offshore of the Coromandel is very sensitive to the source location with wave heights dropping off rapidly as the earthquake deformation is moved further north. The strongest effects result from ruptures occurring just north of East Cape. This effect can be seen in the coarse grid propagation plots shown in Figure 4.3 for source TK 1 and TK 2 with the corresponding near shore maximum water levels

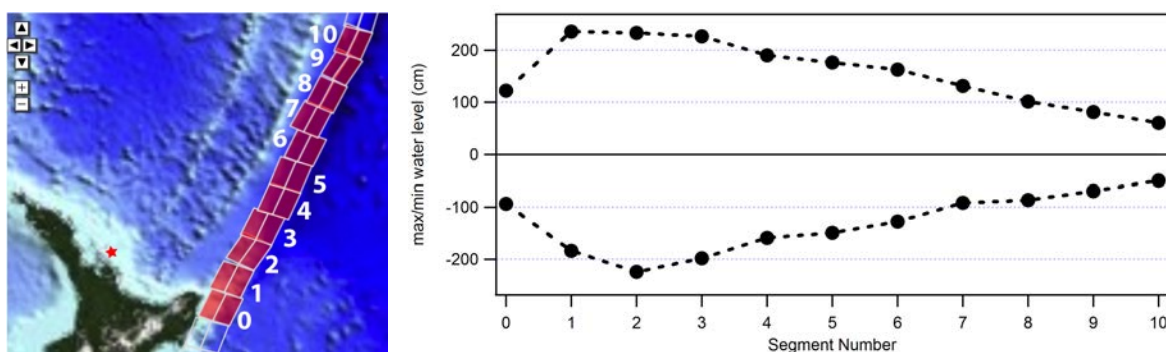


Figure 4.2 Tsunami wave heights produced offshore of the Coromandel Peninsula (red star) by identical tsunami sources positioned on each of the fault segments indicated in the panel on the left. Note that the strongest effects are the result of ruptures in the first 300 km north of the East Cape (segments 1, 2 and 3).

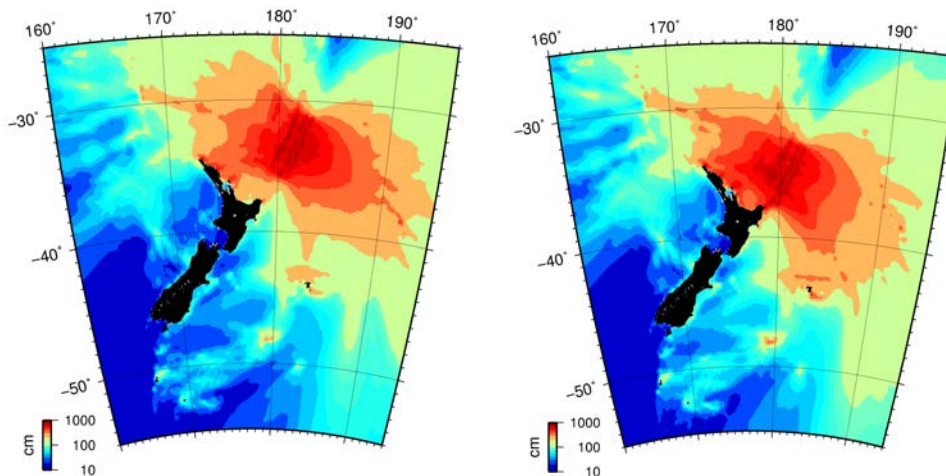


Figure 4.3 Maximum computed tsunami heights over the regional grid for source TK 1 (left) and TK 2 (right). Tsunami heights along the Coromandel Peninsula and in the Bay of Plenty are noticeably higher from source TK 2 due to its more southerly position along the subduction zone.

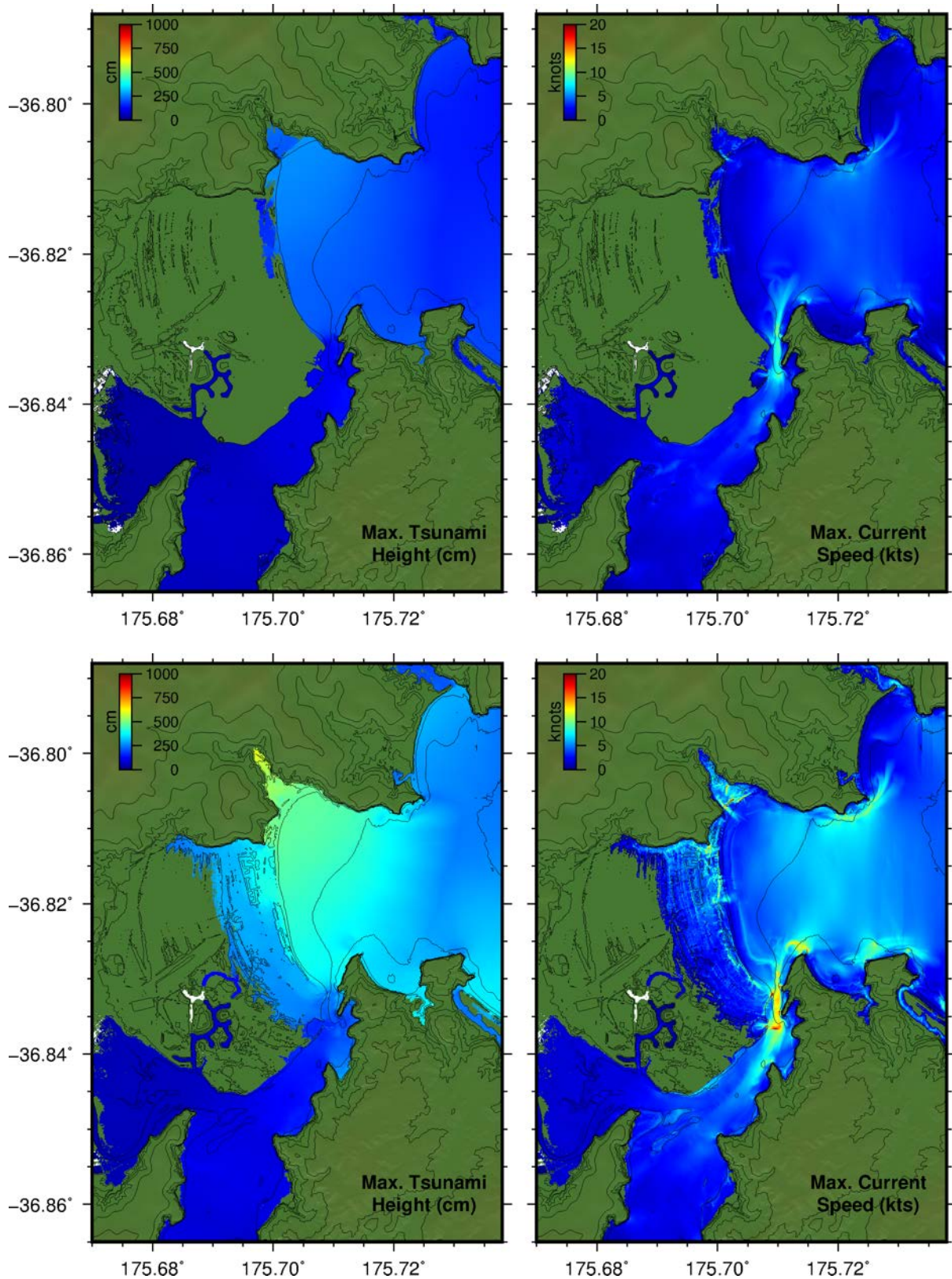


Figure 4.4 Maximum computed tsunami height (left) and current speed (right) for scenarios TK 1 (top) and TK 2 (bottom) in Whitianga; each case run at HT.

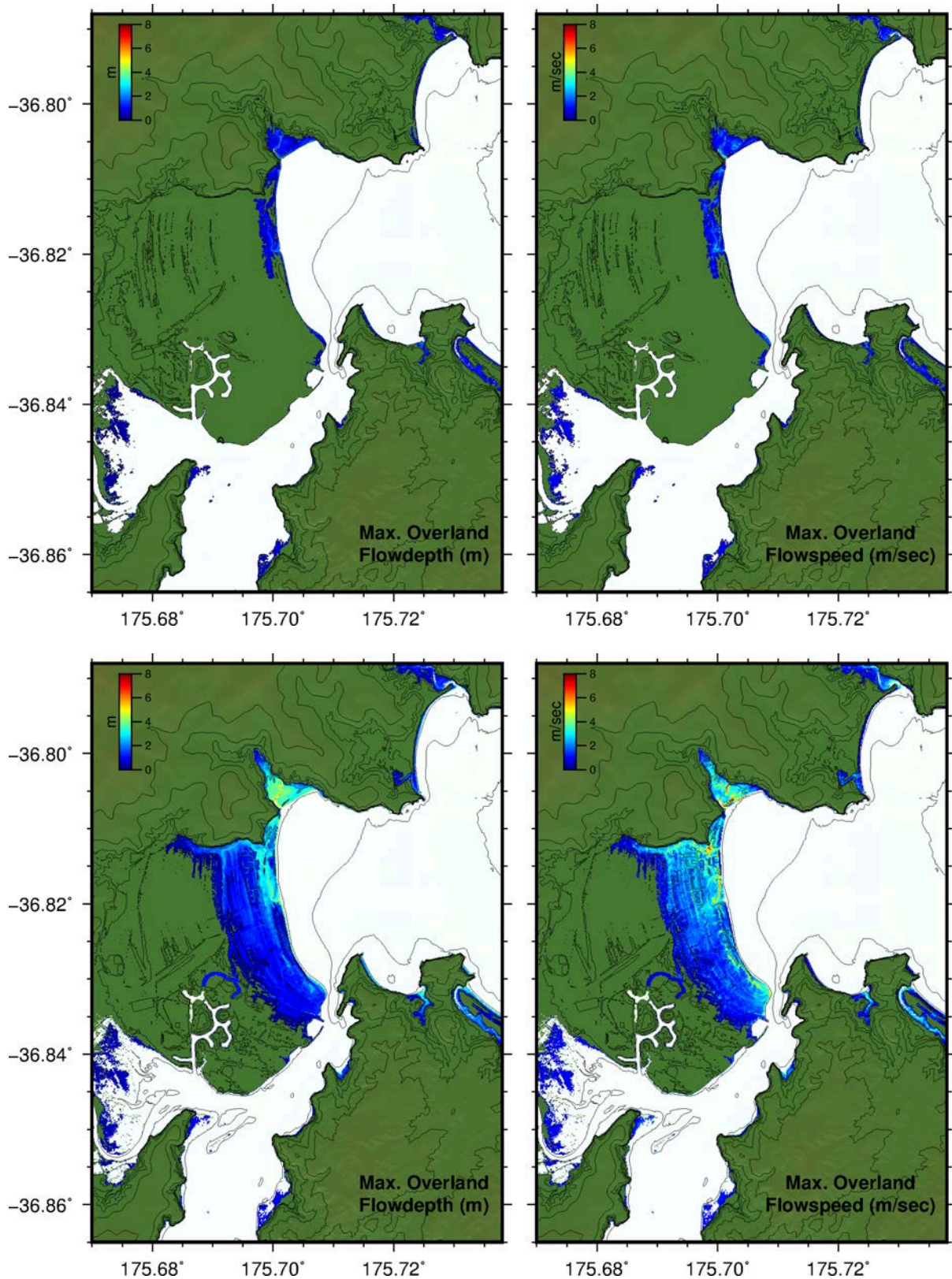
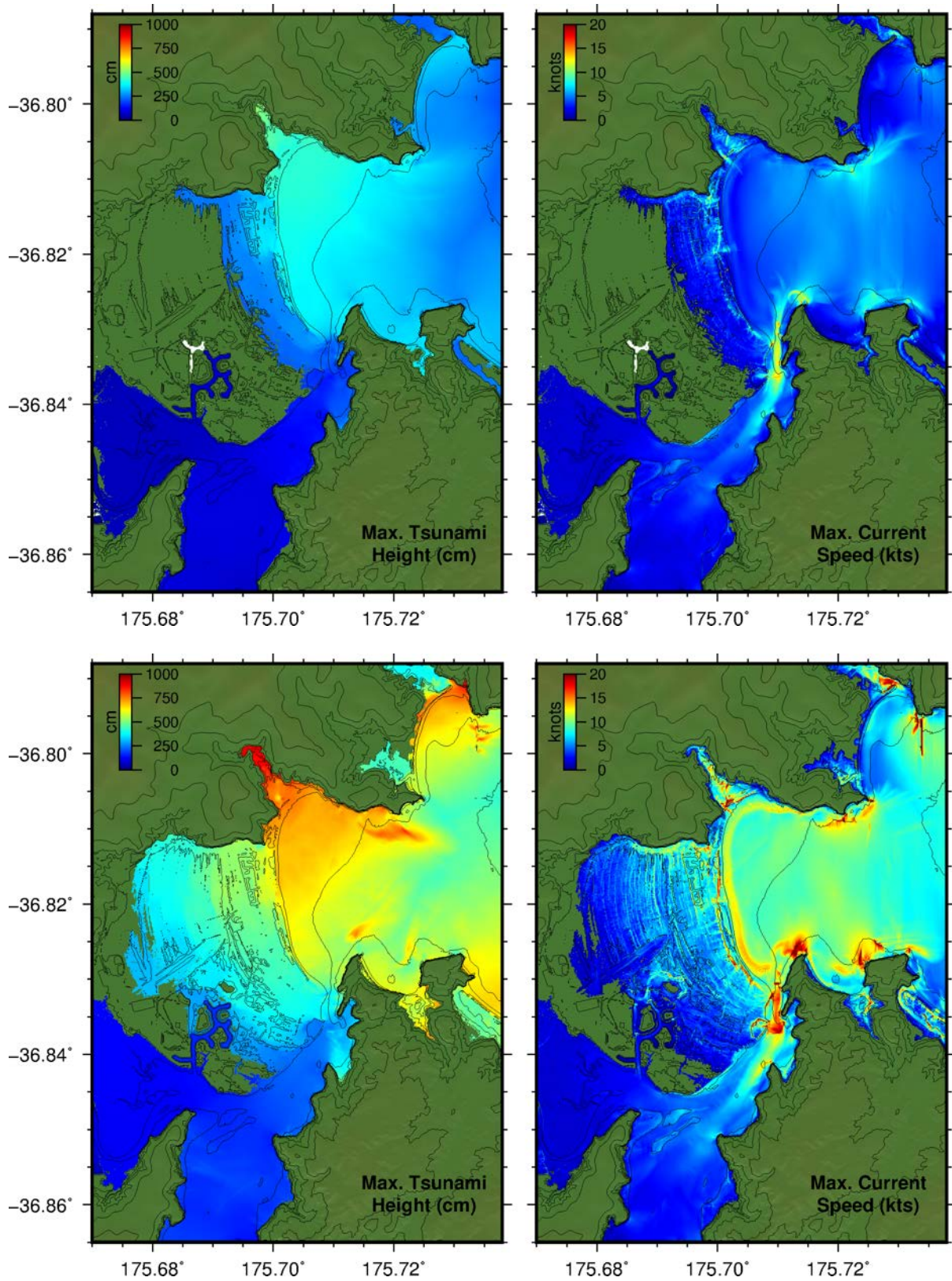


Figure 4.5 Maximum computed overland flow depths (left) and flow speeds (right) TK 1 (top) and TK 2 (bottom) in Whitianga; each case run at HT.



**Figure 4.6** Maximum computed tsunami height (left) and current speed (right) for scenarios TK 7 (top) and TK 8 (bottom) in Whitianga; each case run at HT.

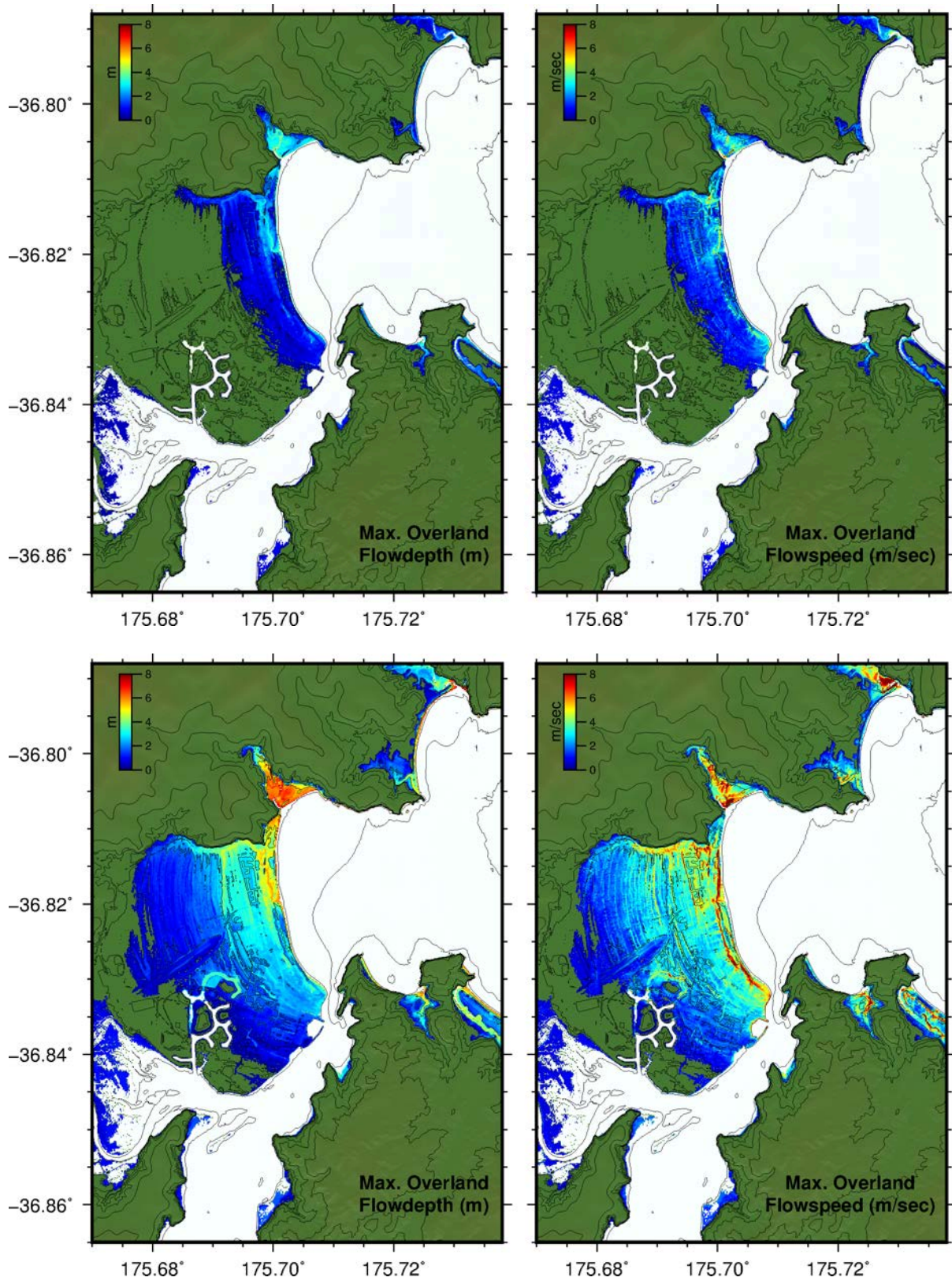
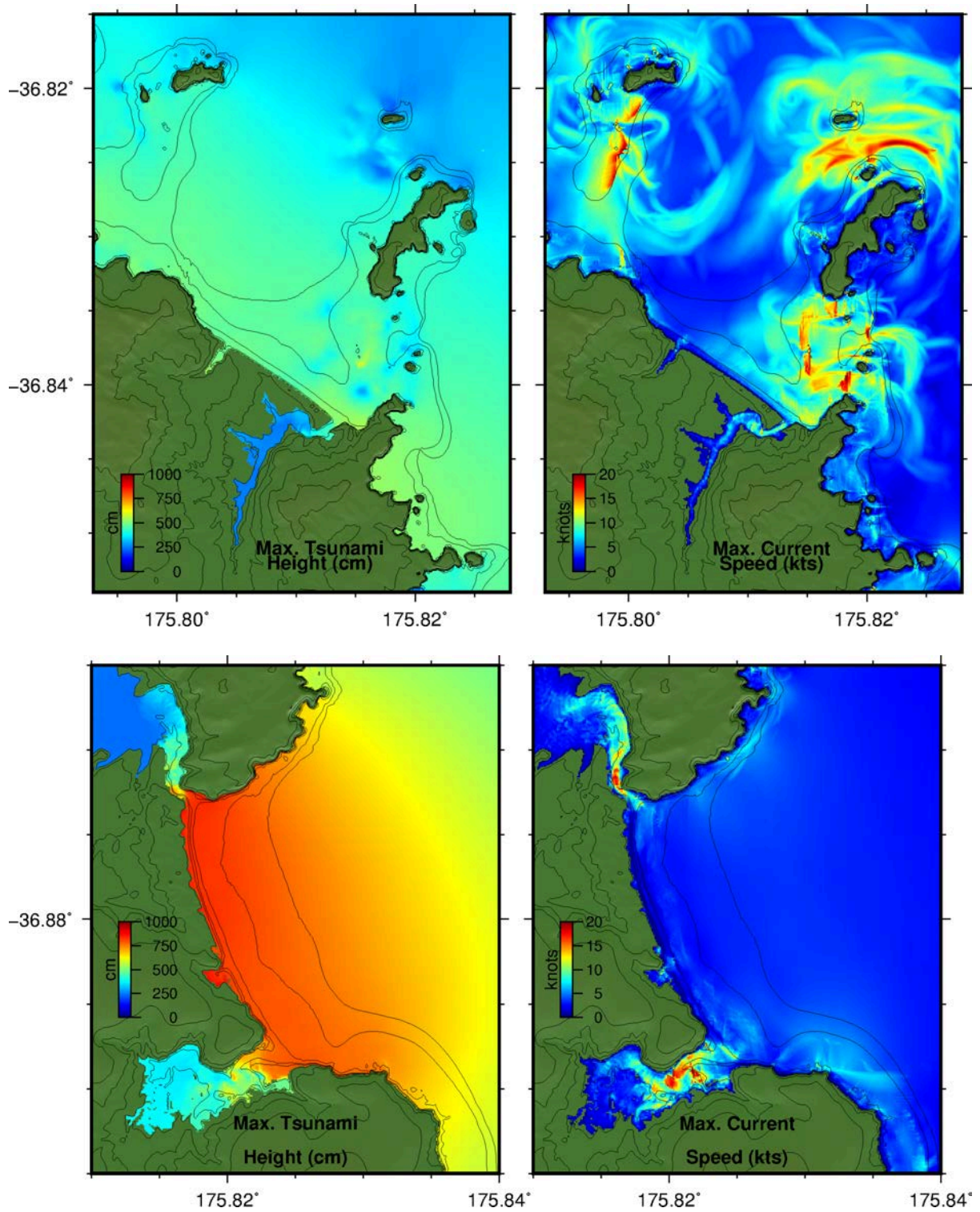
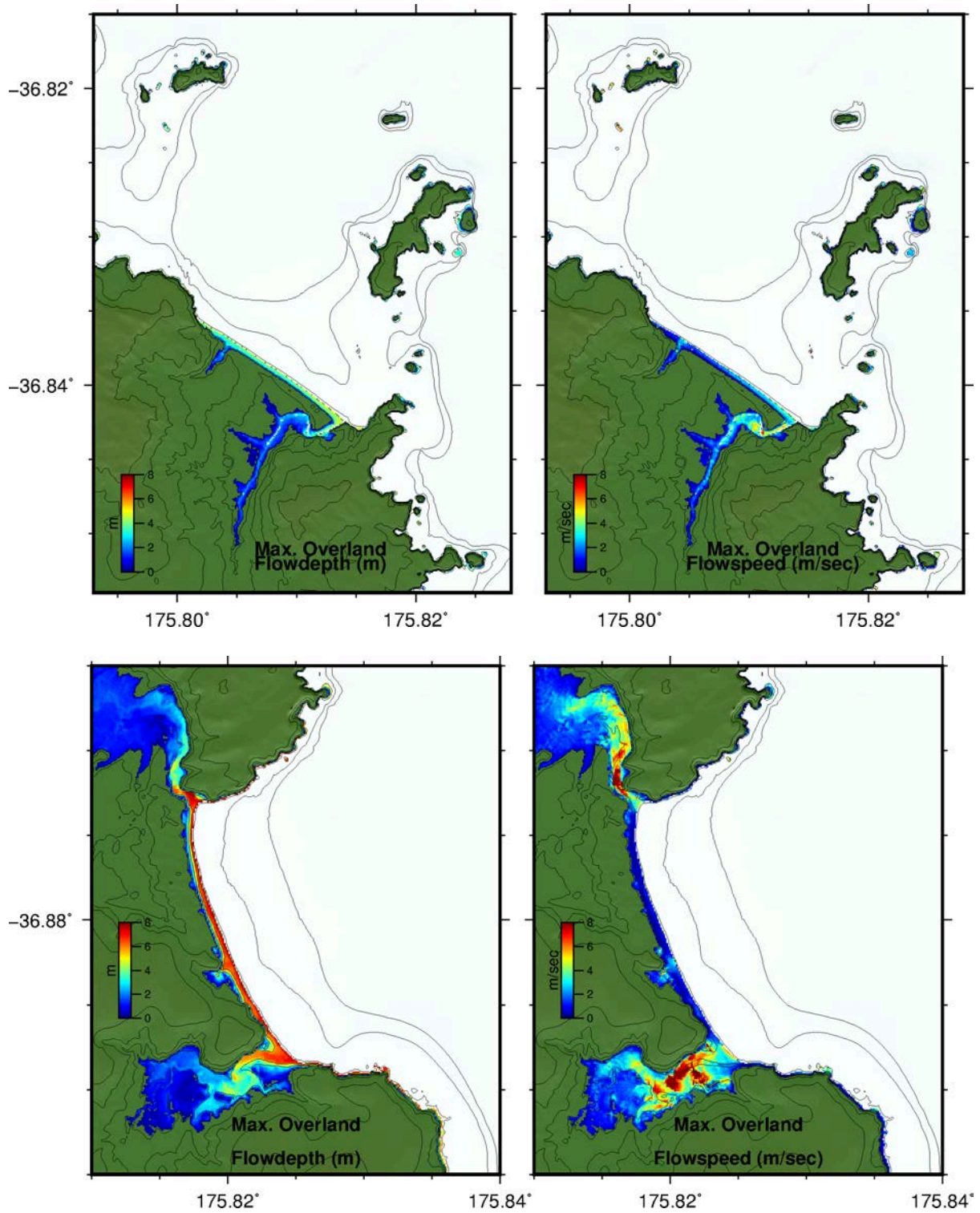


Figure 4.7 Maximum computed overland flow depths (left) and flow speeds (right) TK 7 (top) and TK 8 (bottom) in Whitianga; each case run at HT.



**Figure 4.8** Maximum computed tsunami heights (left) and current speeds (right) at Hahei (top) and Hot Water Beach (bottom) for the TK 8 HT scenario.



**Figure 4.9** Maximum computed tsunami flood depths above ground level (left) and overland flow speed (right) at Hahei (top) and Hot Water Beach (bottom) for the TK 8 HT scenario.

### 4.3 Tsunami Current Speeds

Given the extreme wave heights generated by the TK Trench sources, strong currents would also be expected, particularly through the narrow entrance to Whitianga Harbour. The variations in current speeds at these locations between the least and most severe scenarios (TK 1 and TK 8 respectively) are shown in Figure 4.10.

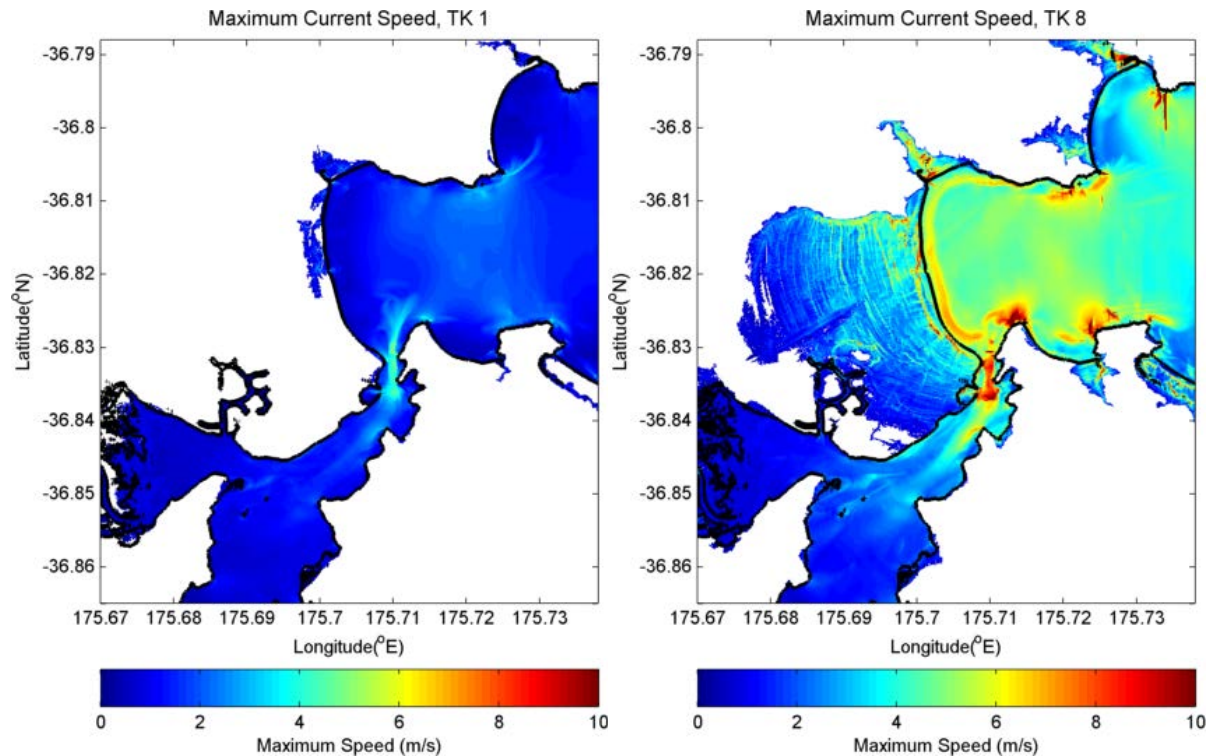


**Figure 4.10 Computed maximum current speeds in Whitianga along Buffalo Beach from scenarios TK 1 (left) and TK 8 (right) at HT.**

Perhaps more important than simply knowing the maximum current speed, the duration of strong currents is also important. This concept is illustrated in the time-current-threshold map shown in Figure 4.11. In this figure, we choose a particular current speed threshold and plot, as a colour, the time (in hours) over which that threshold is exceeded. In this example, we see that for scenario TK 1, the threshold of 3 knots ( $\sim 1.5$  m/s) is exceeded for up to two hours inside the entrance to Whitianga Harbour, while currents exceed this threshold for the full 6 hours of simulation time in the entrance to the harbour and along the shallow headlands on the northern and southern sides of Mercury Bay. In contrast, the TK 8 scenario shows that this 3 knot threshold is exceeded throughout most of Mercury Bay for nearly the entire duration of the model simulation.

We emphasize here that this does not mean currents of this threshold are exceeded continuously over the time duration, but rather, that current speed threshold is exceeded at least once in the time span indicated. The full set of time-current-threshold maps is contained in Appendix 2.

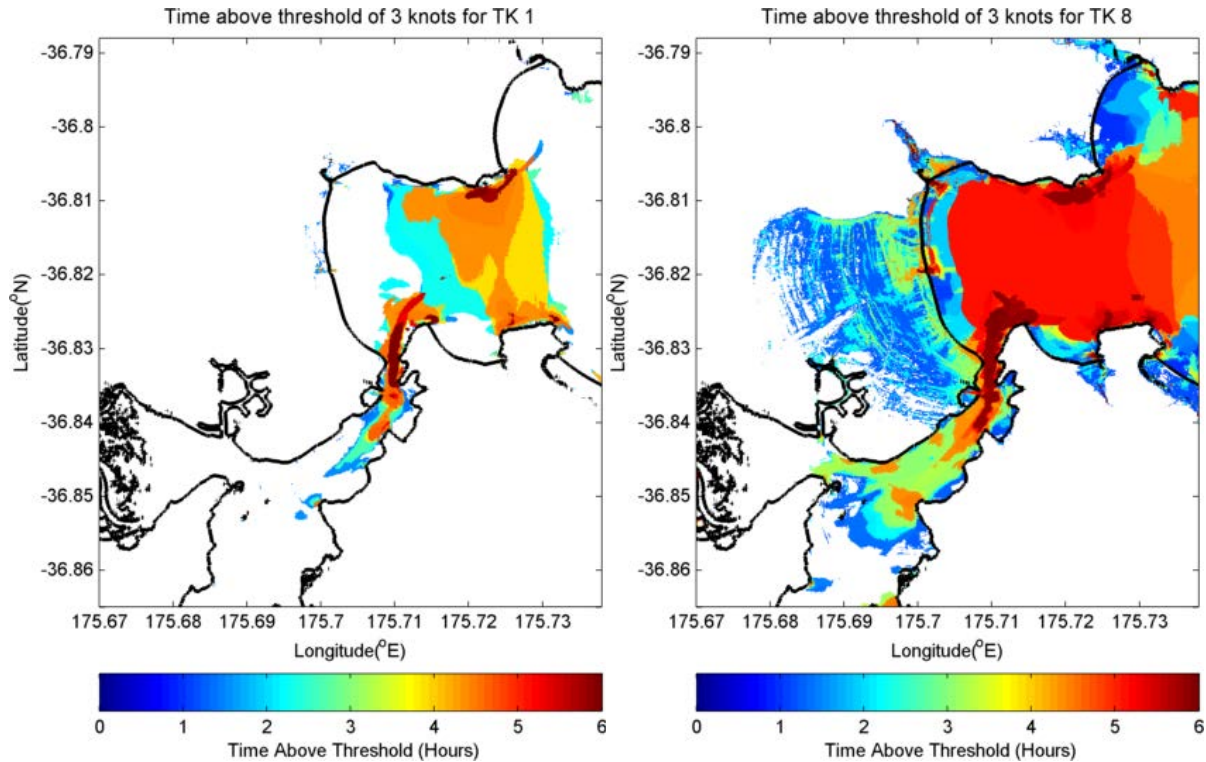


**Figure 4.11 Time-current-threshold maps from scenarios TK1 (left) and TK8 (right) at Whitianga.**

A current hazard plot is presented in Figure 4.12. In this figure we simply plot the maximum computed current speed using a banded colour palette. Presented this way, we can more clearly see which regions of the model domain are susceptible to what level of currents. The complete set of current hazard zone plots is presented for Whitianga in Appendix 2.

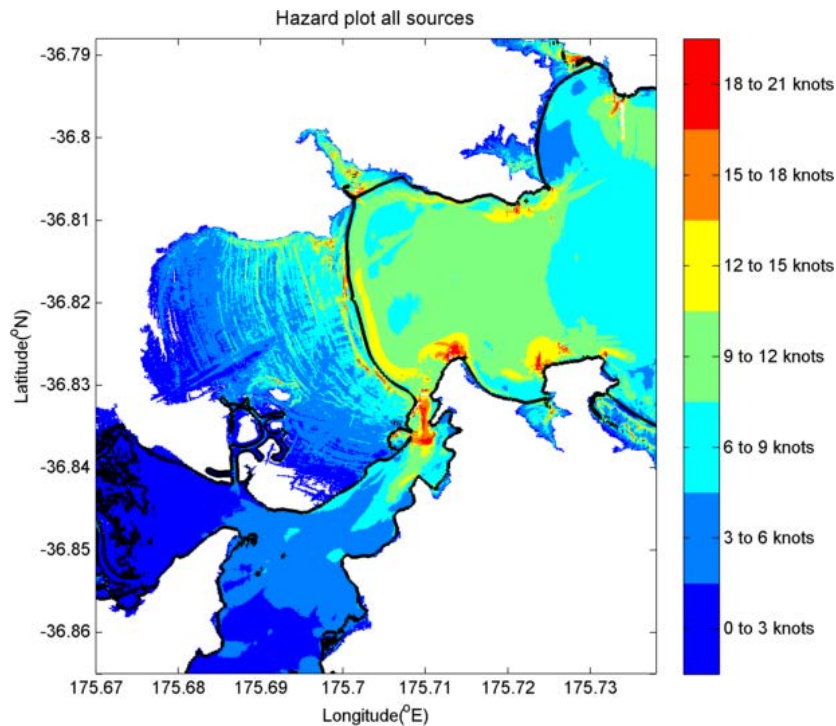


**Figure 4.12 Current hazard zones for Mercury Bay.**

## 5 MODEL RESULTS: DISTANT SOURCE TSUNAMIS

### 5.1 Propagation models

Tsunami inundation, water levels and current speeds for the sources described in Section 2.2 above were modelled at Whitianga and Mercury Bay as well as Hahei and Hot Water Beach. For each of the cases, we have plotted the modelled trans-Pacific tsunami wave heights and the modelled wave heights closer to New Zealand. As shown in Figure 5.1 there is a wide discrepancy in the wave heights between sources with widely disparate magnitudes, i.e. source FF1, the 1960 Valdivia earthquake (M9.5) and source FF2, the 2010 Maule event (M8.8). In Figure 5.2, you can see the different propagation patterns between sources with similar magnitudes located in different areas. It is clear that sources located in the Peru/Chile border region (Chile North 2 and 3 – FF5 and FF6) transmit more tsunami wave energy towards New Zealand than the source located further to the south (Chile North 1, FF4).

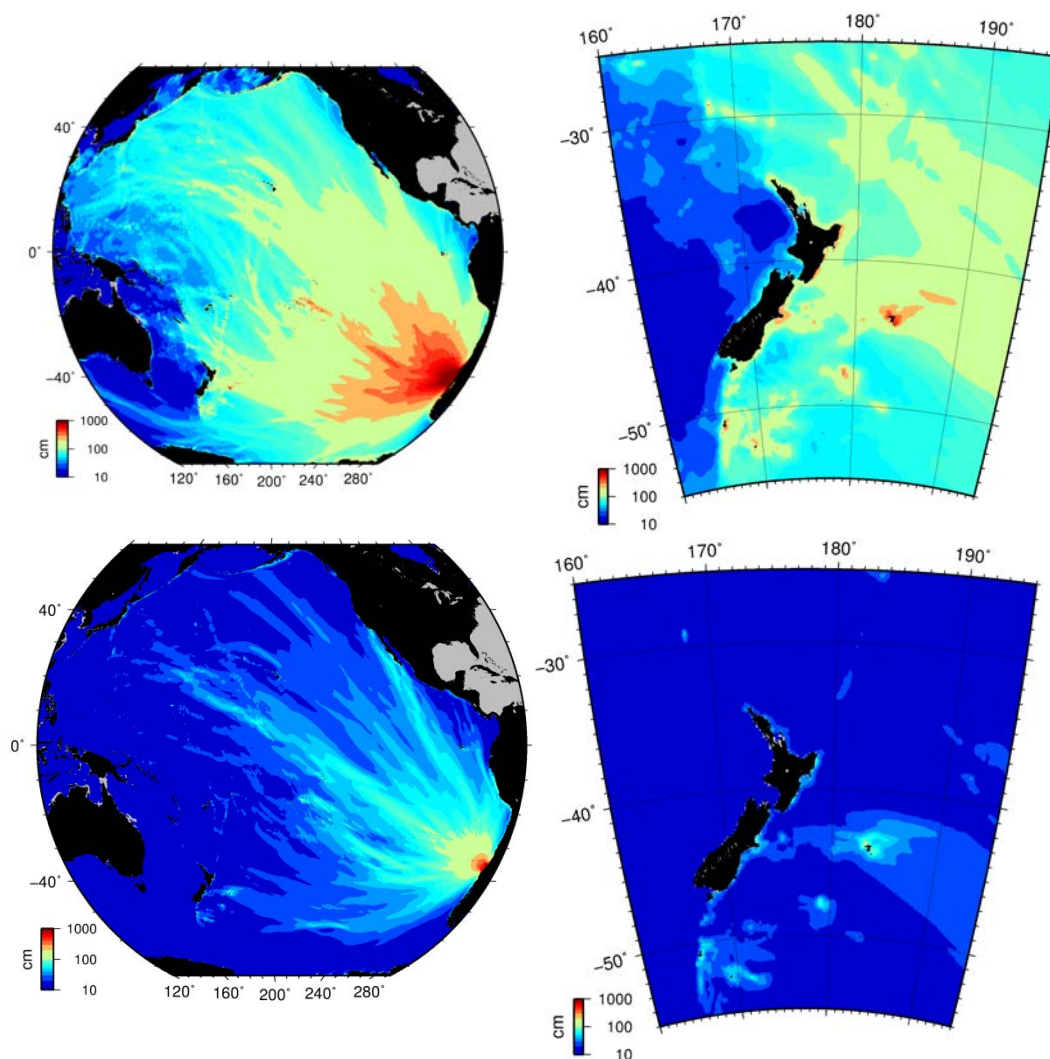


**Figure 5.1 Comparison between trans-Pacific propagation patterns for the 1960 Valdivia, Chile (top) and 2010 Maule Chile (bottom) tsunamis.**

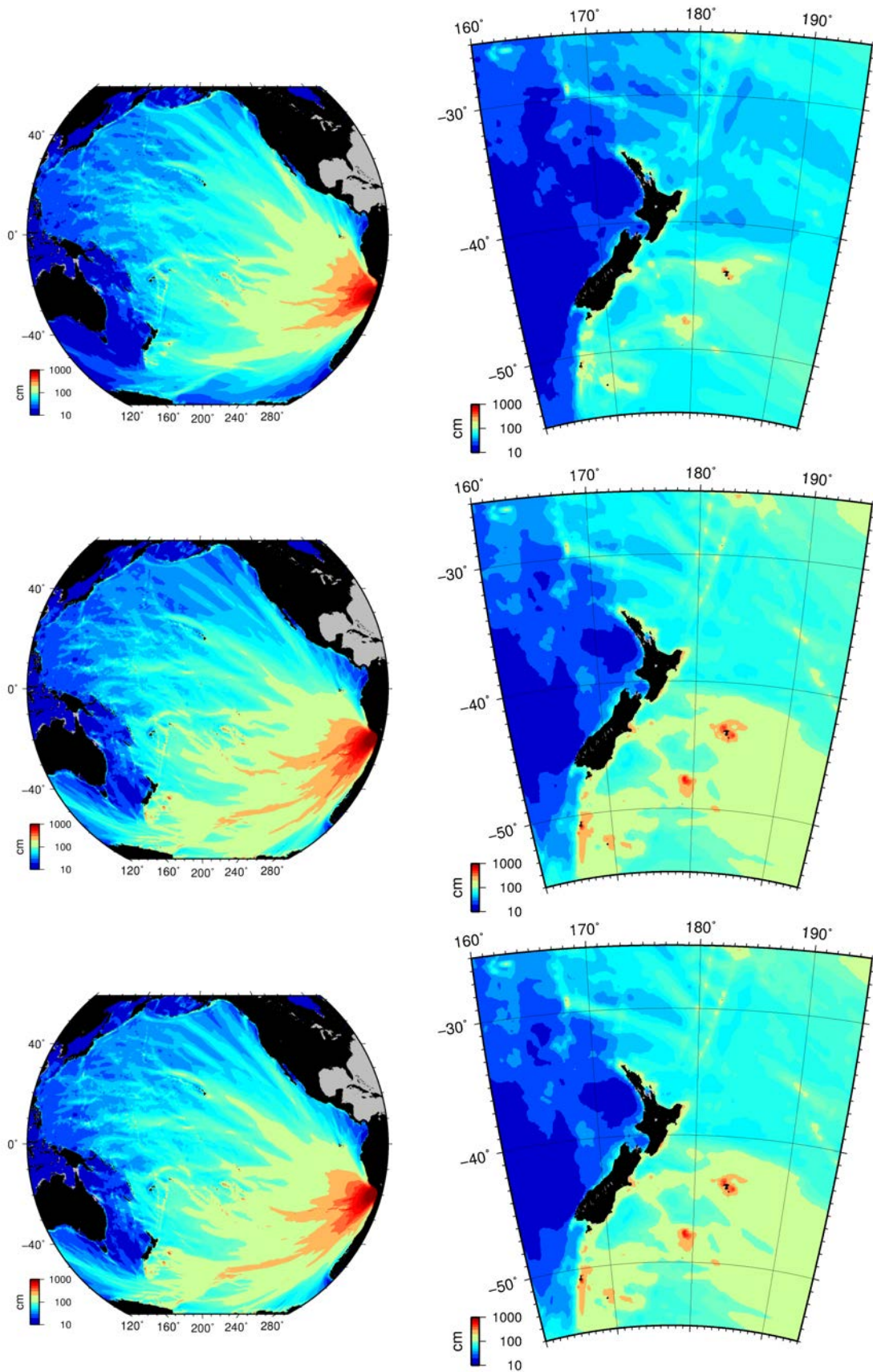


**Figure 5.2 Comparison between trans-Pacific propagation patterns for the three hypothetical northern Chile scenarios: Chile North 1 (top) Chile North 2 (mid) and Chile North 3 (bottom).**

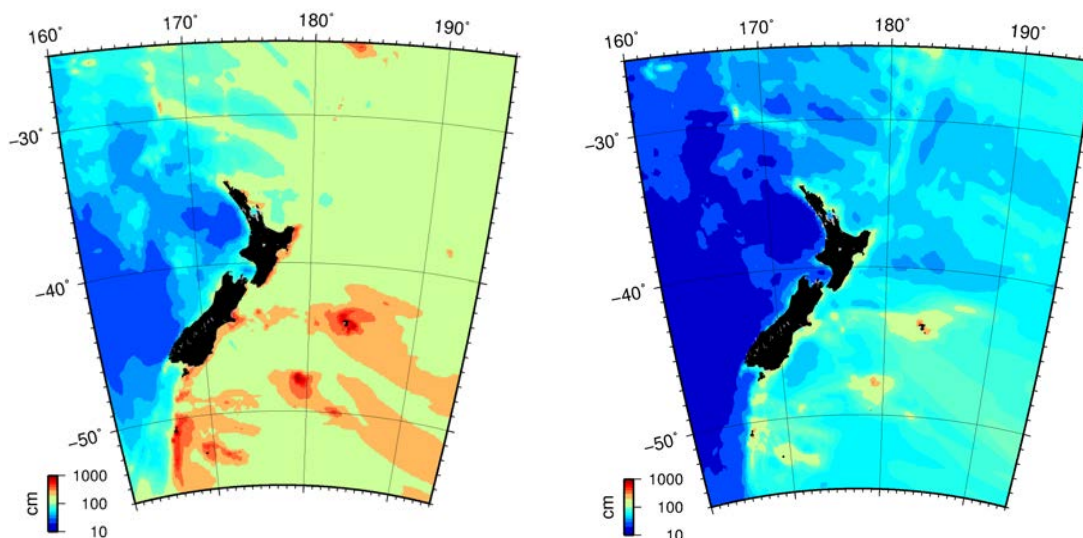


**Figure 5.3 Modelled tsunami heights from the propagation model for the 1868 Arica scenario (left) and the Chile North 1 scenario (right).**

## 5.2 Arrival Times

Modelled time series of water level from a nearshore point at each location for each of the distant source cases is presented in Figure 5.4. Variations in the timing and character of the modelled tsunami waves are evident. We note that sources in southern Chile arrive earlier than do sources located further north. It is also important to note that the largest wave height generally occurs several hours after tsunami arrival, in direct contrast to the regional sources.

## 5.3 Tsunami Heights and Inundation Extents

Modelled tsunami heights from the distant source scenarios for Whitianga and other sites around Mercury Bay are plotted in the following figures (a complete set of the model results is contained in the Appendices). In Figure 5.5 we compare the results from the 1960 Valdivia source to the 2010 Maule Source. It is clear that the 1960 scenario produced much larger wave heights and greater inundation than the 2010 event, consistent with historical accounts.

In Figure 5.6 we compare the model results between the 1868 Arica scenario (Case 3) and the Chile North 1 scenario (Case 4). In this comparison, it is evident that the Chile North 1 scenario (Case 4) produces somewhat larger tsunami heights and greater inundation extents than the 1868 (Case 3) scenario. This is counter intuitive in that the output from the distant source propagation results, shown in Figure 5.3 (above), clearly indicate that the Arica 3 scenario overall produces larger wave heights around New Zealand.

Of the scenarios tested, we found that the Southern Peru (Case 7) scenario produced the greatest tsunami heights and inundation extents of the 8 far field cases (Figure 5.7). We therefore deemed this event to be the Maximum Credible Event for the Whitianga/Mercury Bay area and used it as the source for modelling inundation at the other sites (Hahei and Hot Water Beach) and these results are presented in Figure 5.7. The results show that the inundation extents at the sites that lie outside of Mercury Bay are not as affected by tsunami inundation as are the sites inside Mercury Bay (Buffalo Beach, Cooks Beach and Wharekaho) however there is still

appreciable inundation extending up the low lying river and creek outlets and the Hahei area is particularly affected by strong currents rushing through and around the offshore islands and reefs.

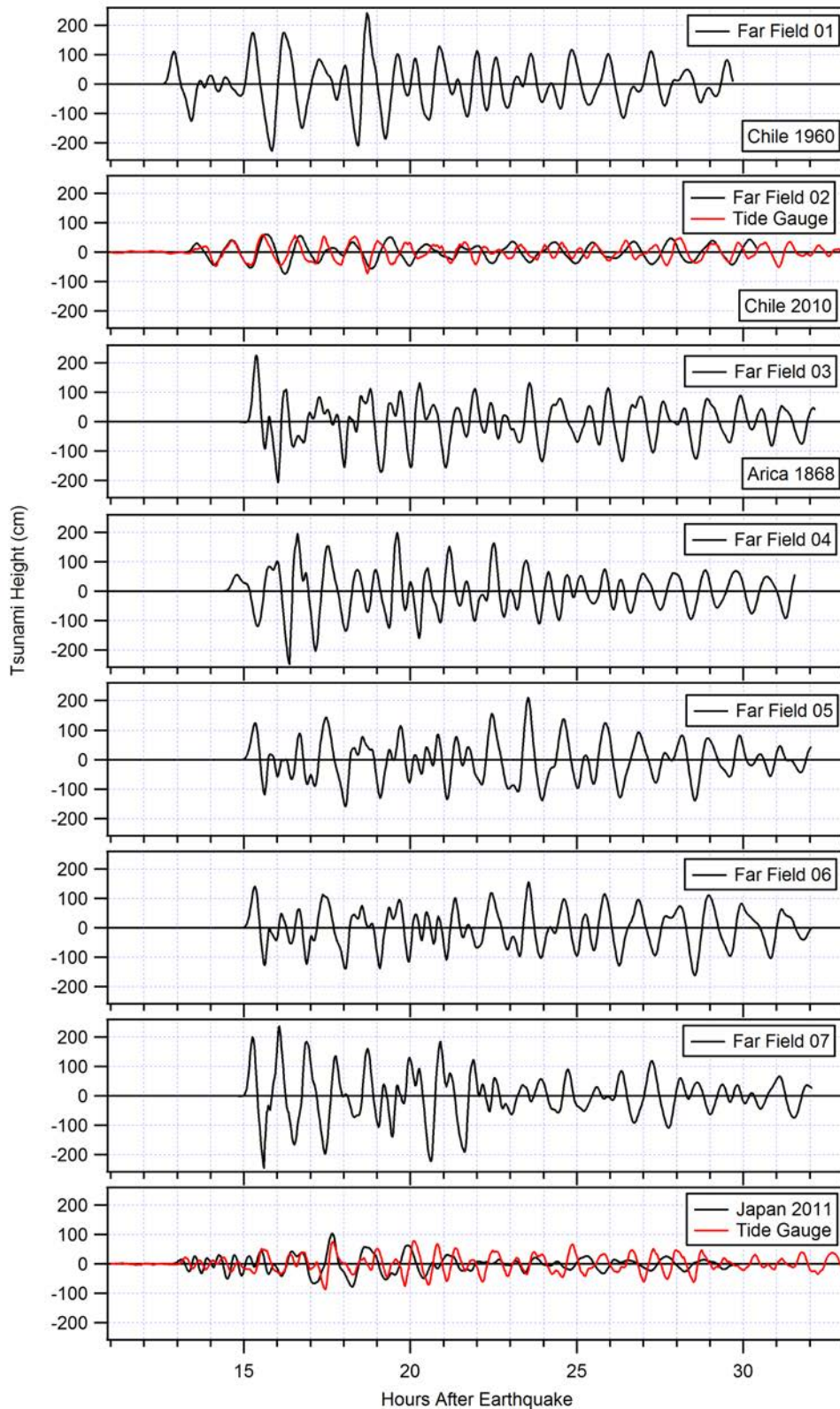


**Figure 5.4 Modelled time series of water levels offshore of Buffalo Beach for each of the distant source scenarios. Measured tide gauge data plotted in red.**

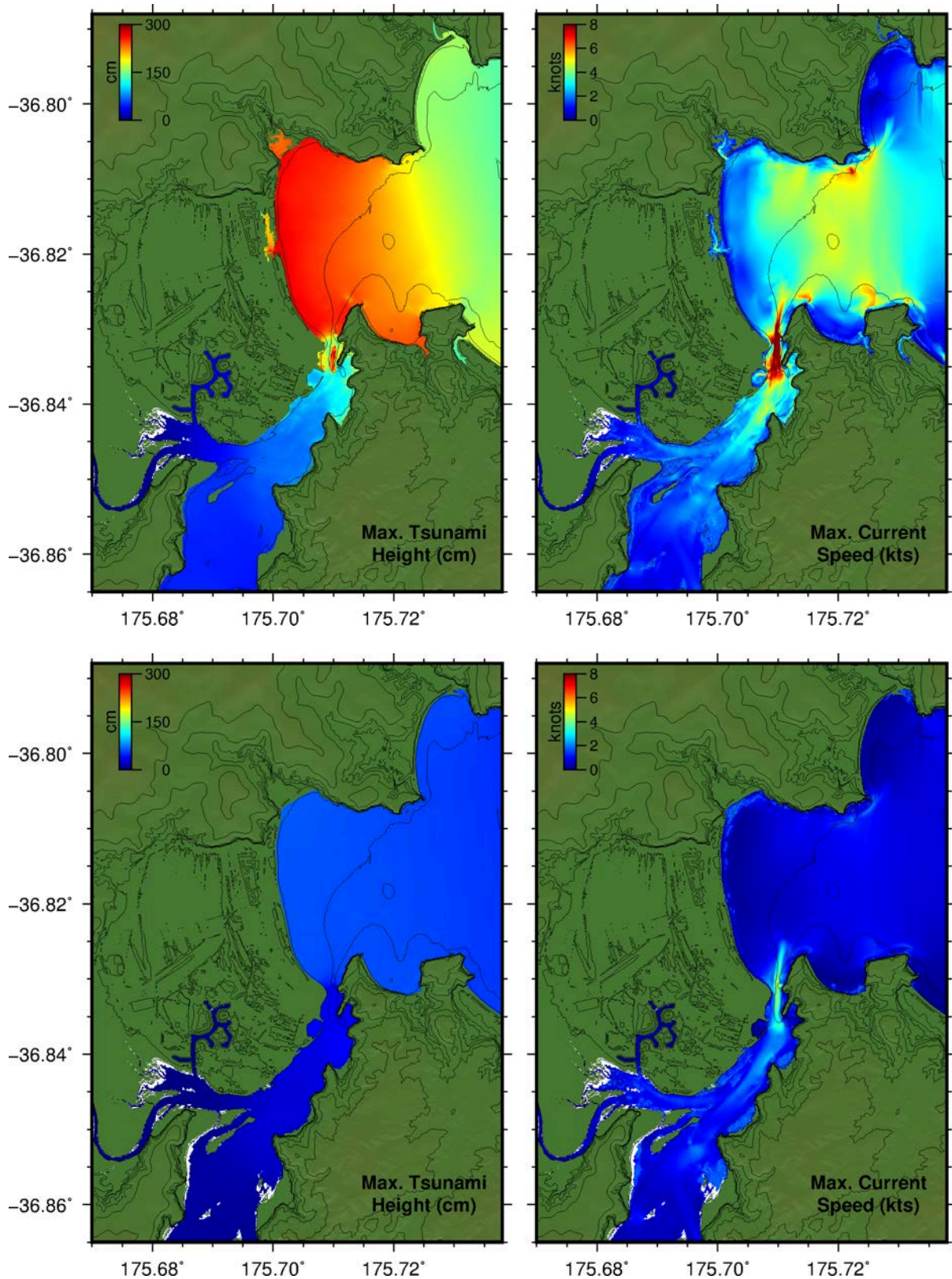
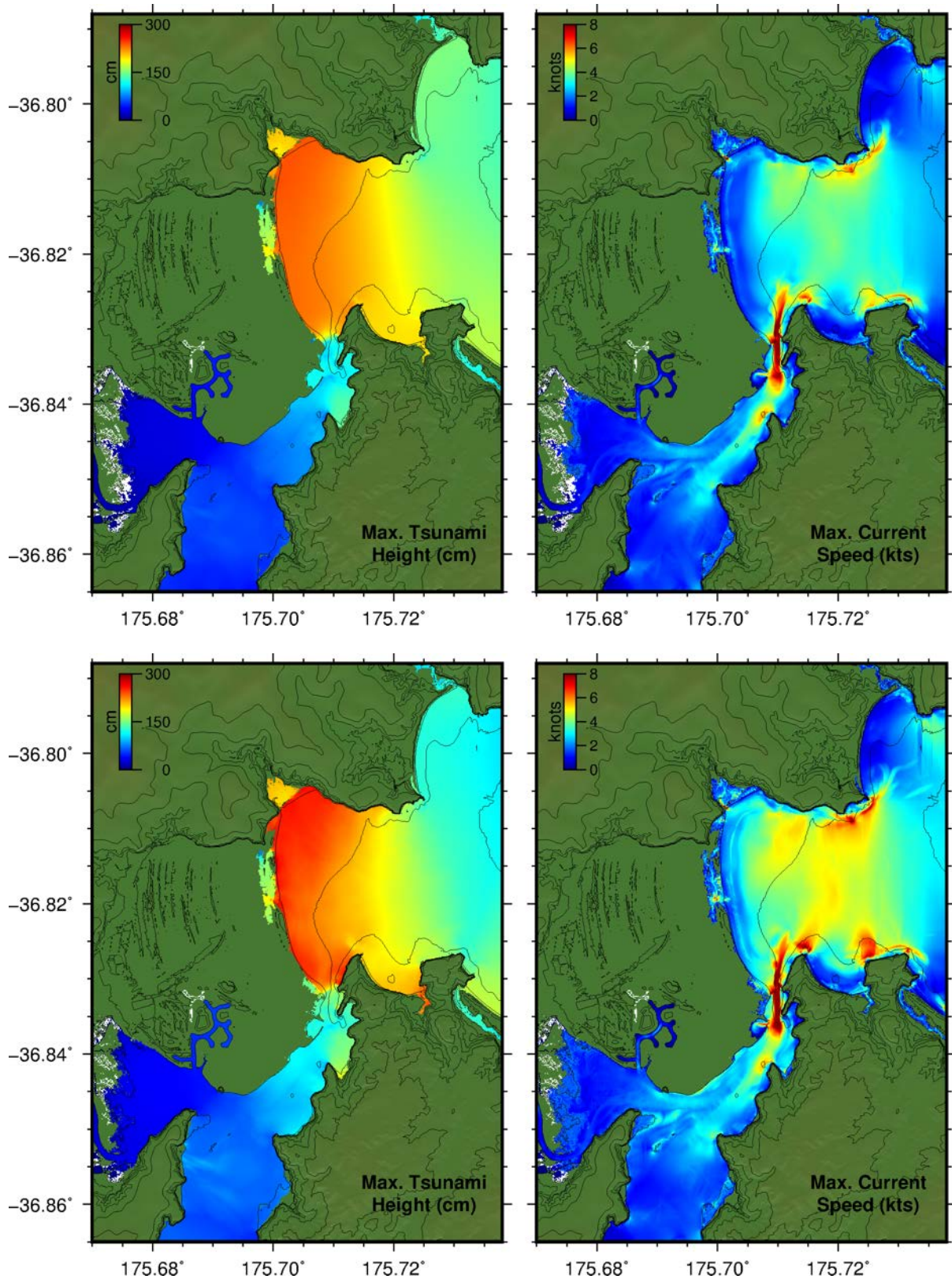
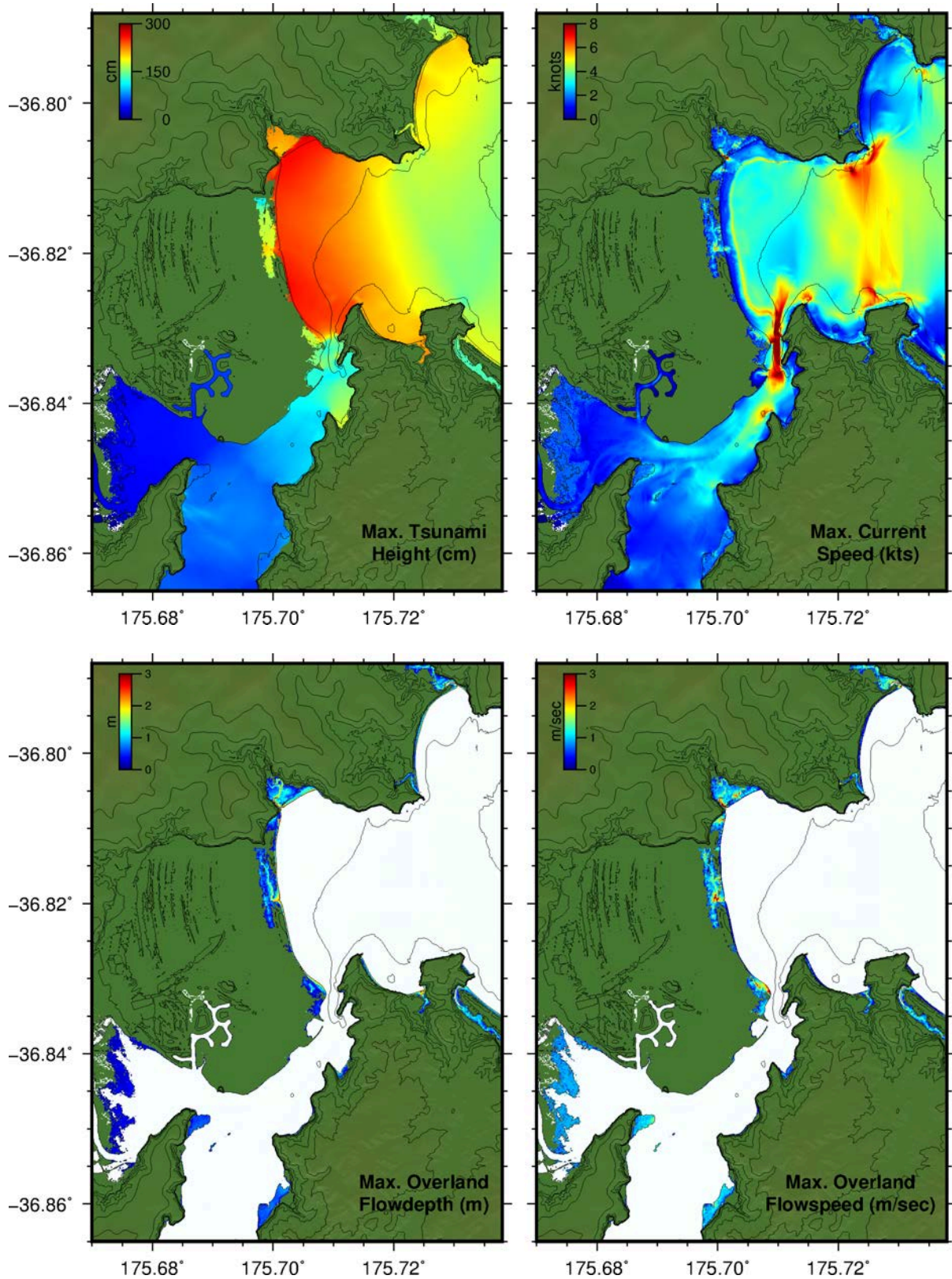


Figure 5.5 Modelled tsunami heights (left) and current speeds (right) from the 1960 Valdivia Chile scenario (FF1) at mid tide (top) and for the 2010 Maule Chile scenario (FF2) at mid tide (bottom) for Whitianga and Buffalo Beach.



**Figure 5.6 Modelled tsunami heights (left) and current speeds (right) from the 1868 Arica scenario (FF3) (top) and the Chile North 1 (FF4) (bottom) at high tide for Whitianga and Buffalo Beach.**



**Figure 5.7 Modelled tsunami heights (top left) current speed (top right) flow depth (bottom left) and overland flow speed (bottom right) for the Southern Peru (FF 7) scenario at High tide.**

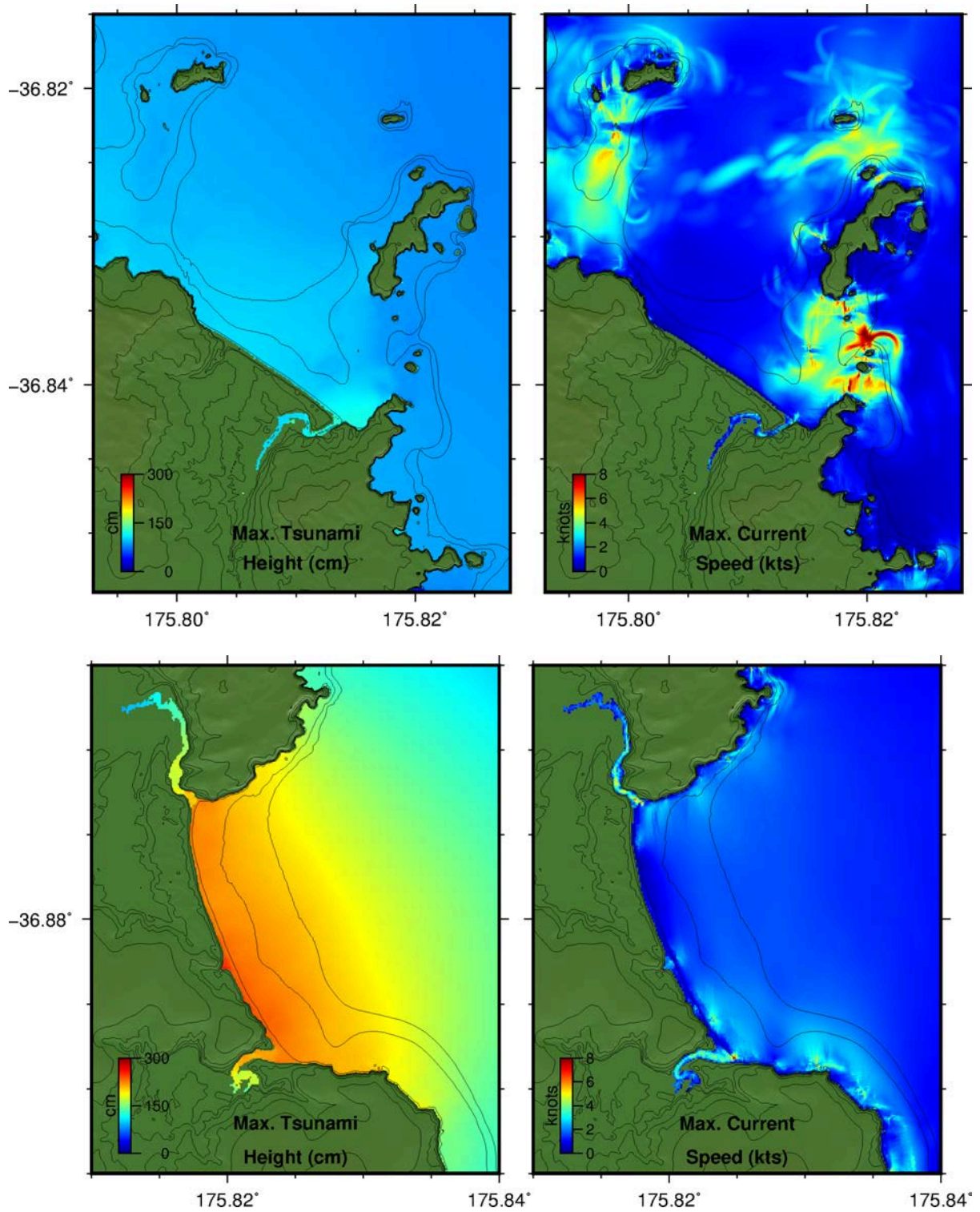


**Figure 5.8 Modelled tsunami heights (left) and current speeds (right) for Hahei (top) and Hot Water Beach (bottom) for the Southern Peru (Case 7) scenario.**

#### 5.4 Tsunami Current Speeds

As with the TK Trench scenarios, we consider both maximum current speed as well as the duration of these currents. For the distant source scenarios, the duration of strong currents is more important than in the near source cases since the largest tsunami heights occur later in the tsunami time series. In terms of the maximum current speeds, the results from the two largest scenarios, Arica 1868 and Central Peru, are shown in Figure 5.9. We see that the maximum current speeds are in the order of 5 m/s (~10 knots) and occur primarily at the entrance to the Whitianga Harbour and along the northern and southern headlands at the entrance to Buffalo Bay.

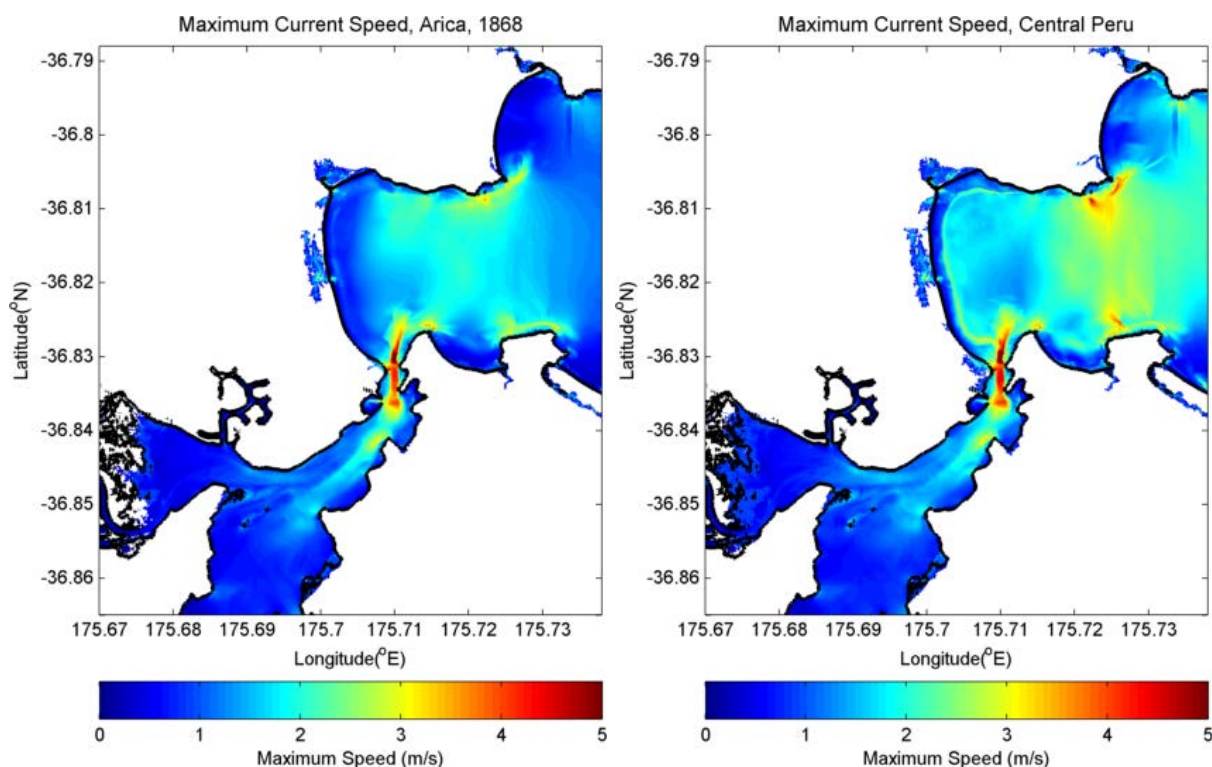


**Figure 5.9** Maximum modelled current speeds from the Arica 1868 (left) and Central Peru (right) scenarios for Whitianga at HT.

In terms of the current duration, the plots in Figure 5.10 suggest that current speeds greater than 3 knots would persist at the entrance to Whitianga Harbour and between the Islands for up to 16 hours after tsunami arrival. Finally, in Figure 5.12 the high current speed hazard zones are defined across all distant source tsunami scenarios tested in this study.

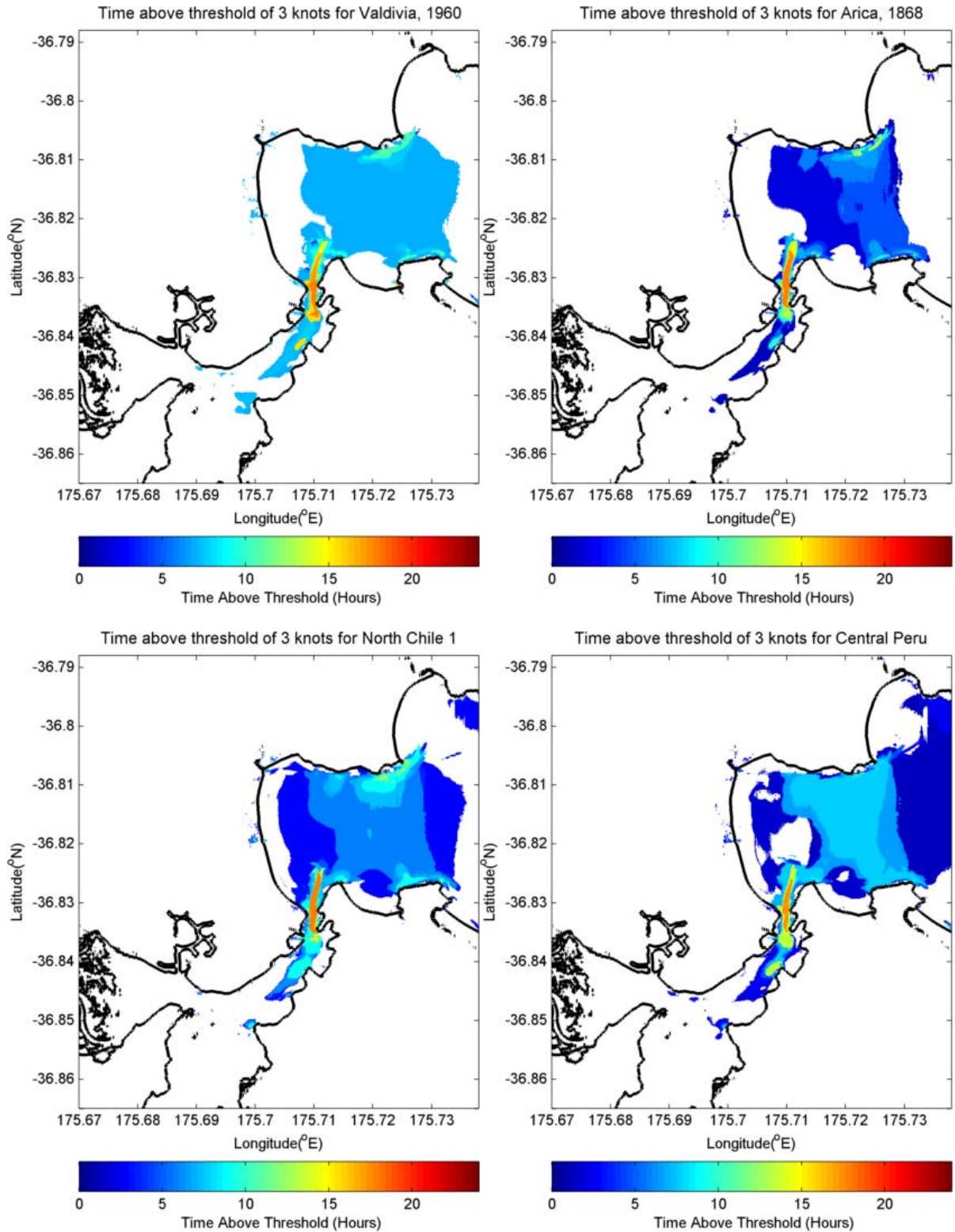


**Figure 5.10 Time Current threshold maps for current speeds of 3 knots for the Chile 1960 (top left) Arica 1868 (top right), Chile North 1 (bottom left) and Central Peru (bottom right) at High tide in Whitianga and Buffalo Bay.**

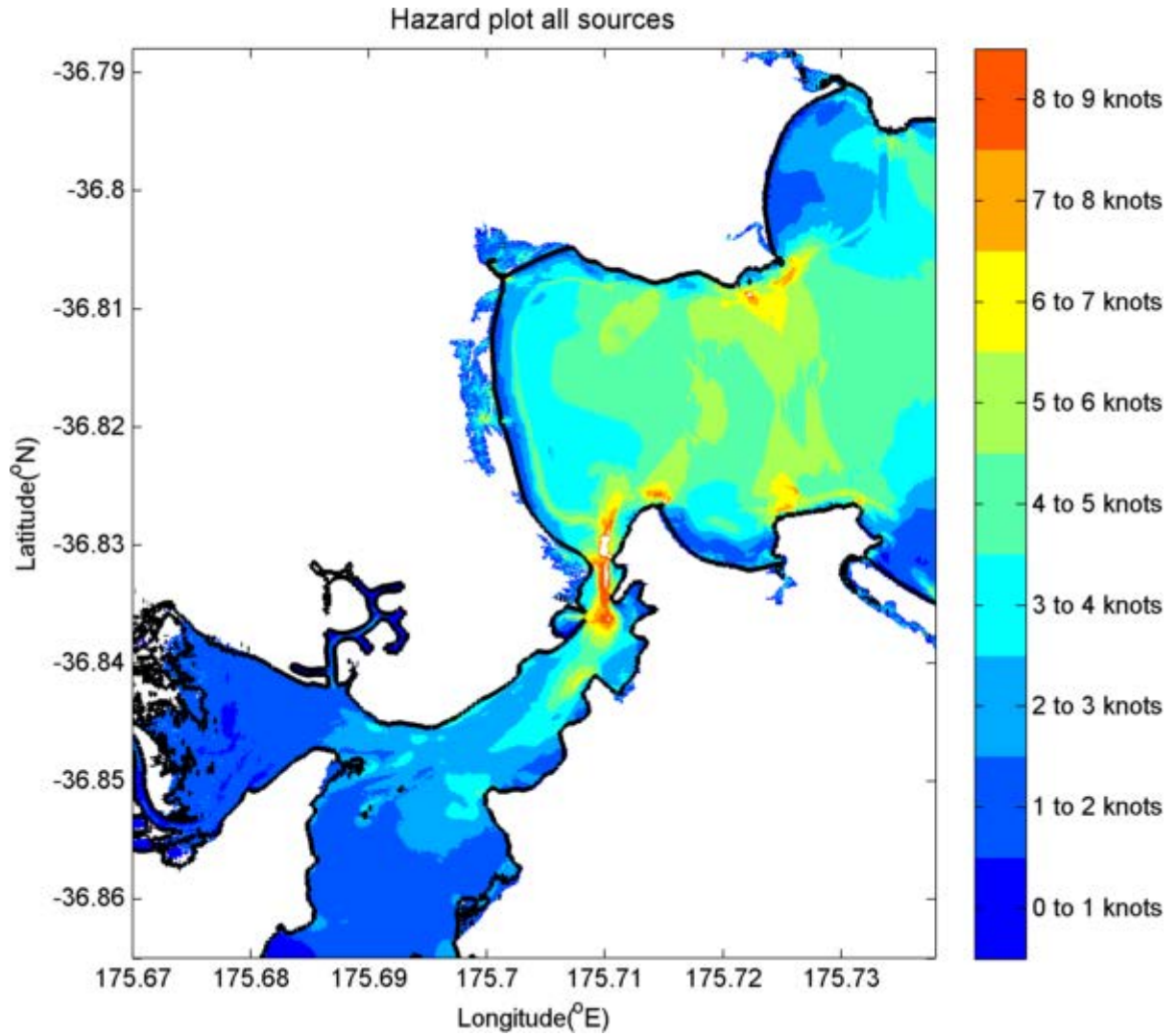


**Figure 5.11 Current hazard zones for Whitianga showing areas where strong currents would be expected during large far-field tsunamis.**

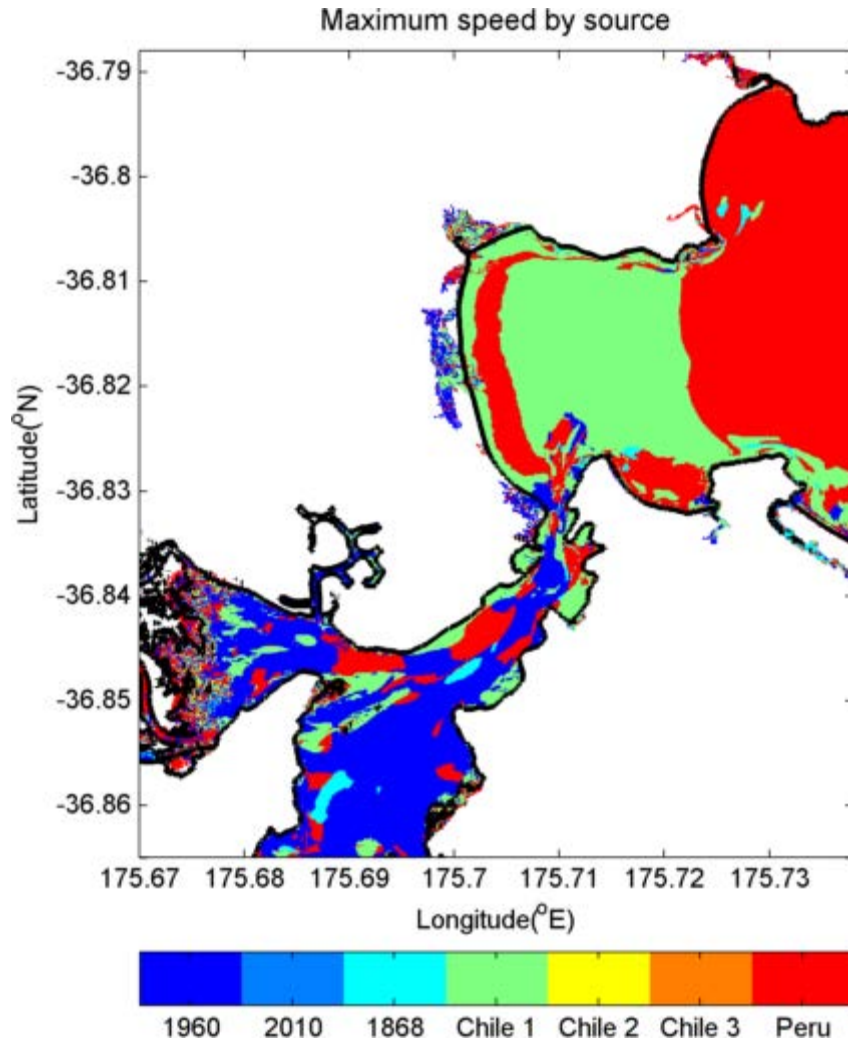


Figure 5.12 Maximum modelled current speeds as a function of the tsunami source.

## 6 MODEL SENSITIVITY: FRICTION COEFFICIENT

Due to the extreme inundation predicted for Whitianga during the Tonga Kermadec scenarios, we tested the model sensitivity to the friction coefficient. For all of the model runs completed to date, we have used a uniform friction coefficient (Manning  $n$ ) of 0.03. This value is chosen as the default value recommended by NOAA/PMEL for the ComMIT modelling system and is based on numerous trials of ComMIT (and the MOST model) for use in modelling tsunami inundation. This friction value was used in the study by Wei et al (2012) to successfully model the inundation extents along the Japanese coast from the 2011 Tohoku tsunami.

For this comparison we use the TK 8 scenario, which incidentally is the same source mechanism used in the Wei et al., 2012 study. For the sensitivity test we ran the model at three friction settings of 0.03, 0.035 and 0.04 and compare the inundation extents and current speeds for each.

In Figure 6.1 we plot time series of water level from just offshore of Buffalo Beach for the three cases and in Figure 6.2 and Figure 6.3 we present the inundation extents, current speeds, flow depths and overland flow speeds for the different friction settings.

As expected the increasing friction coefficient results in reduced water levels and flow speeds. However, the differences mostly affect the inland extents of the inundated area while tsunami heights and flow depths near the shoreline are largely similar across the three runs.

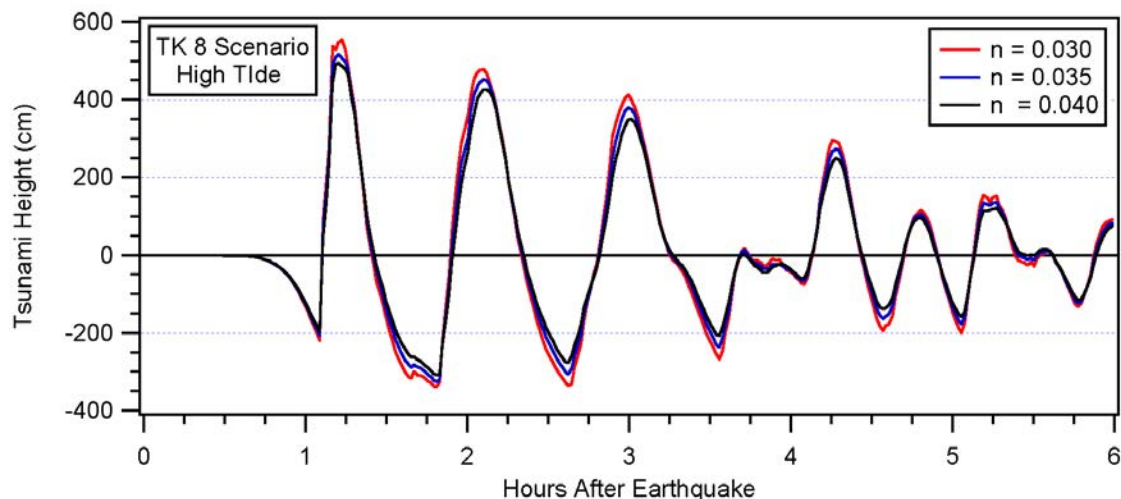
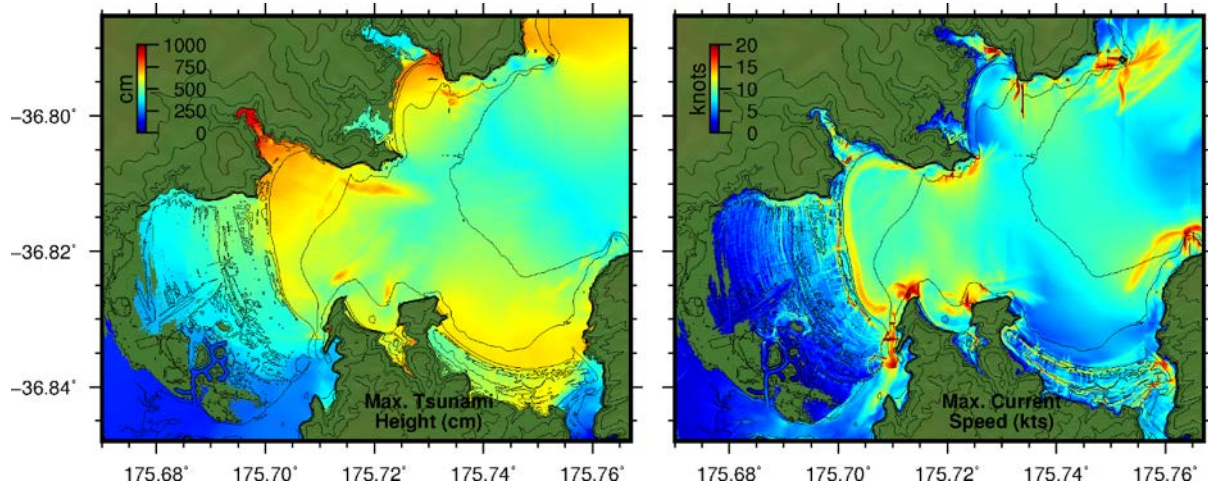
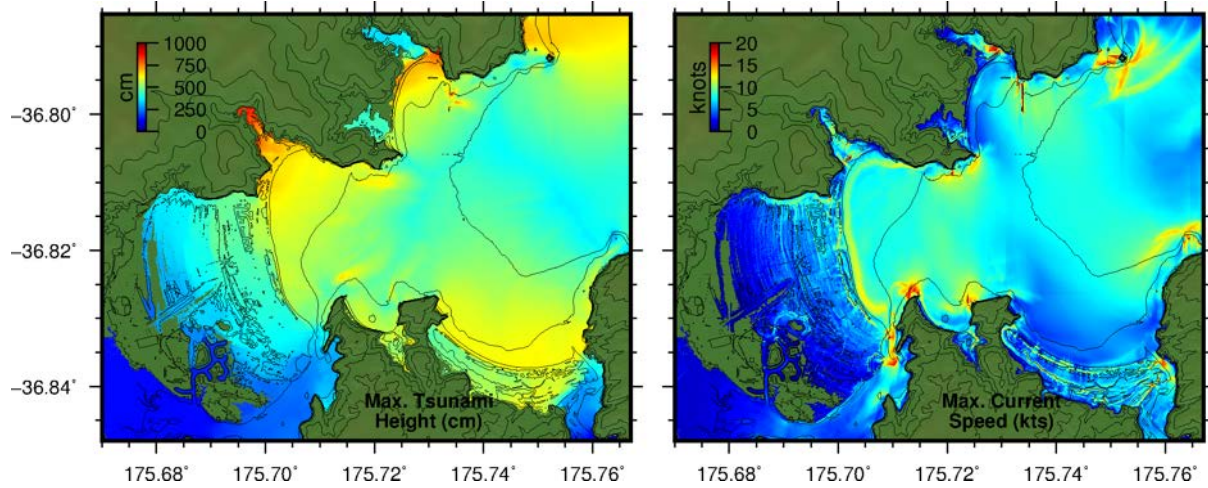


**Figure 6.1 Modelled water levels offshore of Buffalo Beach for the TK \* scenario at High Tide with three friction coefficients.**

$n = 0.030$



$n = 0.035$



$n = 0.040$

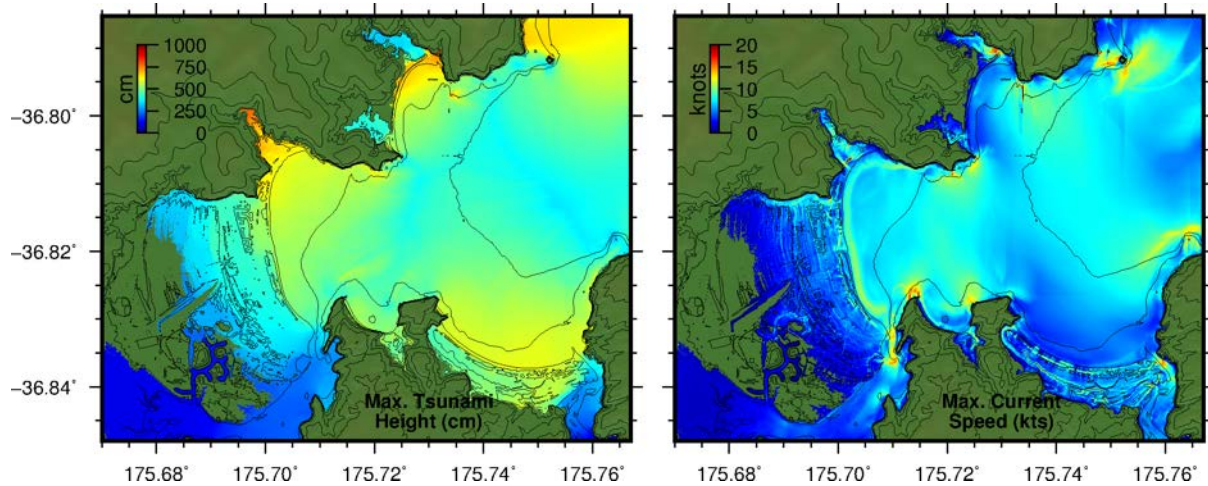
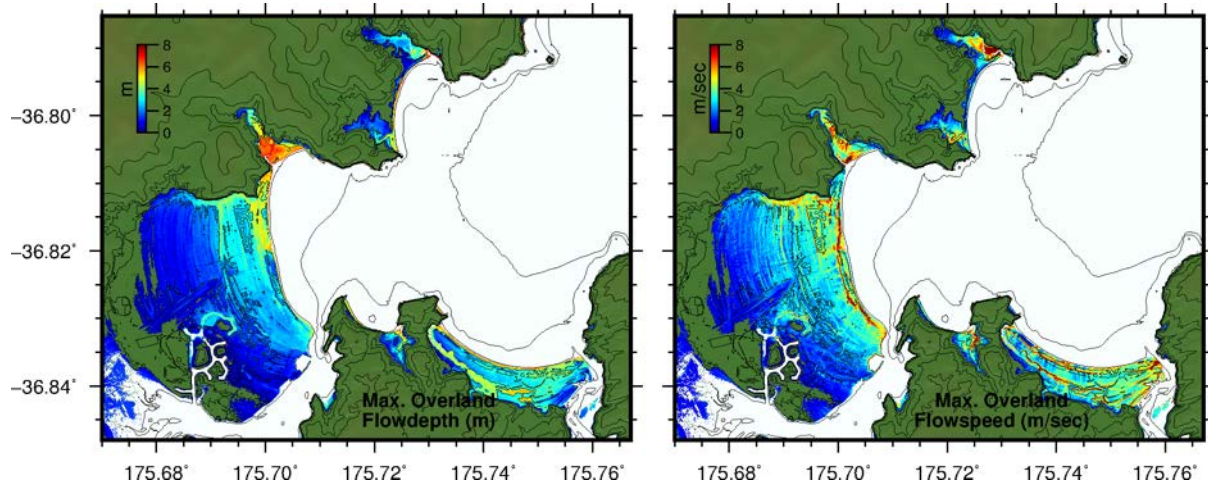
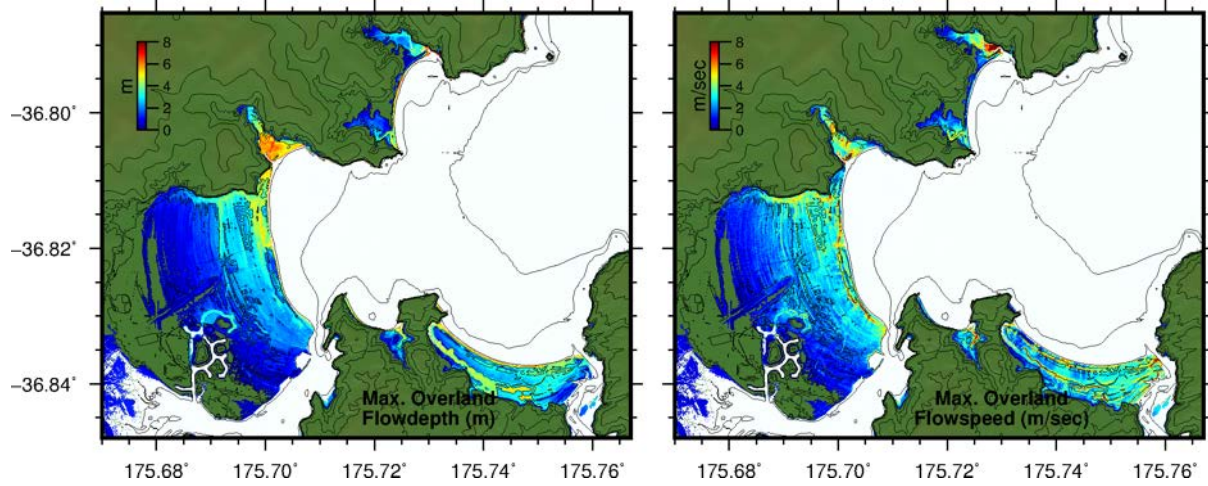


**Figure 6.2 Modelled inundation extents and offshore current speeds in Whitianga as a function of different friction coefficients.**

$n = 0.030$



$n = 0.035$



$n = 0.040$

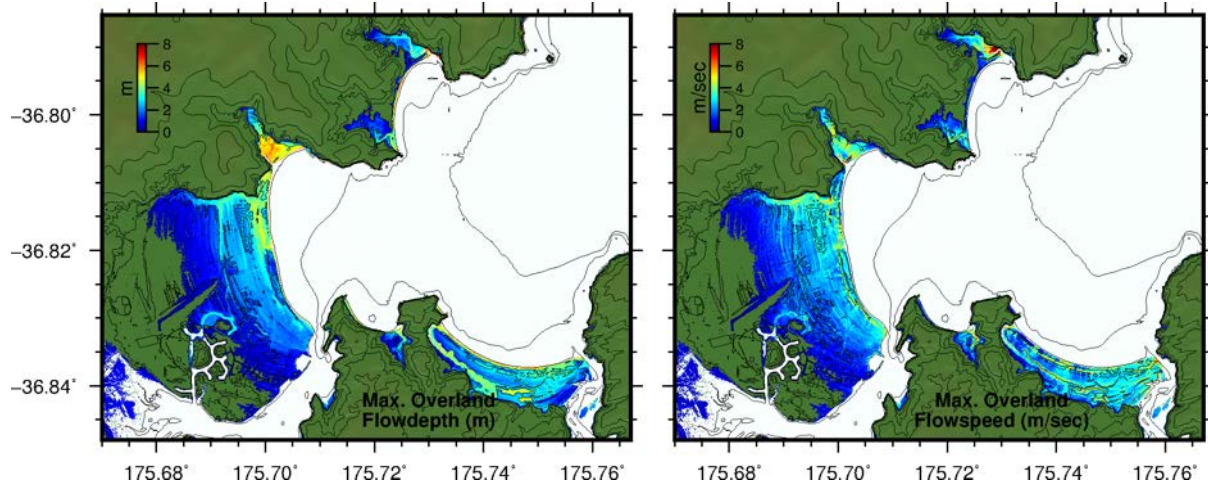


**Figure 6.3 Modelled overland flow depths (left) overland flow speeds in Whitianga as a function of different friction coefficients.**

## 7 SUMMARY AND CONCLUSIONS

We have evaluated the tsunami hazard for Whitianga and the Mercury Bay area including Buffalo Beach, Cook's Beach, Wharekaho, the entrance to Whitianga Harbour, Hahei and Hot Water Beaches. The assessment includes tsunami inundation, overland flow depths and tsunami induced current speeds.

For the regional sources we focus on the Tonga-Kermadec (TK) Trench and model a suite of 8 scenarios comprised of four different earthquakes at two different locations. Earthquake magnitudes range from M 8.8 to M 9.1 and consider both uniform and distributed slip scenarios. Of the cases modelled, each of the cases causes appreciable overland inundation along Buffalo Beach. This is in contrast to previous modelling studies for other areas along the Coromandel Peninsula that were not inundated by the smaller TK source events.

The arrival time from these regional sources is relatively short. Initial drawdown of the sea level begins, approximately 45-60 minutes after the earthquake and reaches its maximum drawdown at 60-75 minutes after the earthquake. The first peak of the tsunami wave train was the largest in each of the scenarios and reached its maximum value at 75 minutes after the earthquake. In general the subsequent tsunami wave peaks were reduced in height relative to the first peak.

The modelled tsunami currents speeds were, as expected, greatest for the largest magnitude source positioned closest to the study area (i.e. TK 8) with currents in excess of 20 knots modelled at the entrance to Whitianga Harbour. However, even the smaller sources (TK1 and TK 2) produced significant current at the harbour entrance and along the rocky headlands to the north and south of Buffalo Bay.

At Hahei and Hot Water Beaches, the TK 7 and TK 8 scenarios produced significant inundation along the beach front and up the creek outlets that exist at each beach.

An important difference between the Whitianga/Buffalo Beach results and modelling results at other sites in the area (i.e. Whangamata, Tairua, Pauanui, Kennedy Bay, Opito Bay Kuaotunu and Whangapoua) is that the Buffalo Beach area experiences significant inundation for each of the TK trench scenarios. In previous studies, significant inundation was only seen for the larger earthquake magnitudes positioned at the southernmost location along the TK trench (north of East Cape). This result shows the extreme vulnerability of Whitianga and Buffalo Bay to tsunami effects.

For the distant source scenarios, we consider several large magnitude (M 8.8 to 9.4) earthquake sources along the South American subduction zone. Three of these sources are based directly on historical events (1868 Arica, 1960 Valdivia and 2010 Maule Chile events). The remaining four scenarios use an earthquake source model based on the 1960 Valdivia event that is positioned at different locations along the coast of South America. We also present results from the 2011 Japan tsunami.

For the 1960 Valdivia scenario, we modelled the inundation in Whitianga and along Buffalo Beach at mid and high tide and showed that the inundation extents roughly correspond to the observed inundation that occurred in that area in 1960.

Of the scenarios tested, we found that the Central Peru (FF 7) scenario produced the greatest tsunami heights and inundation extents of the 8 far field cases. We therefore deemed this event to be the Maximum Credible Event for the Whitianga/Mercury Bay area and used it as the source for modelling inundation at the other sites (Hahei and Hot Water Beach). The results show that the inundation extents at the sites that lie outside of Mercury Bay are not as affected by tsunami inundation as are the sites inside Mercury Bay (Buffalo Beach, Cooks Beach and Wharekaho) however there is still appreciable inundation extending up the low lying river and creek outlets and the Hahei area is particularly affected by strong currents rushing through and around the offshore islands and reefs.

In terms of tsunami induced current speeds, the distant source scenarios produce lower peak current speeds than the extreme regional source, however, the duration of the currents is much longer, with current speeds of more than 2 knots persisting for more up to 16 hours after tsunami arrival.

Again, these model results show considerably more inundation and stronger currents in Whitianga and along Buffalo Beach for tsunami sources that did not cause significant tsunami effects at other sites in the area further highlighting Whitianga's tsunami vulnerability.

These model results will be used by the Thames-Coromandel District Council and the Waikato Regional Council as part of evacuation planning and emergency management activities as well as for education and outreach activities amongst the potentially affected populations.

## 8 REFERENCES

- Borrero, J.C. (2013). *Numerical modelling of tsunami effects at two sites on the Coromandel Peninsula, New Zealand: Whitianga and Tairua-Pauanui*, (Waikato Regional Council Technical Report No. 2013/24, (Vol. 4355, pp. 1–96).
- Borrero, J.C. (2014). *Numerical modelling of tsunami effects at Whangamata, Whiritoa and Onemana, Coromandel Peninsula New Zealand*, Report prepared for the Waikato Regional Council, September 2014.
- Borrero, J.C. and Greer, S.D. (2012) Comparison of the 2010 Chile and 2010 Japan tsunamis in the Far-field, *Pure and Applied Geophysics*, 170, 1249-1274, DOI 10.1007/s00024-012-0559-4.
- Borrero J.C. and Goring D.G (2015) South American Tsunamis in Lyttelton Harbor, New Zealand, *Pure and Applied Geophysics*, Volume 172, Issue 3, pp 757-772.
- Borrero, J.C., Goring, D.G., Greer, S.D. and Power, W.L. (2014) Far-Field Tsunami Hazard in New Zealand Ports, *Pure and Applied Geophysics*, Volume 172, Issue 3, pp 731-756.
- De Lange, W.P., & Healy, T.R. (1986). New Zealand tsunamis 1840–1982. *New Zealand Journal of Geology and Geophysics*, 29(1), 115–134. doi:10.1080/00288306.1986.10427527
- Dorbath, L., A. Cisternas, and C. Dorbath (1990). Assessment of the size of large and great historical earthquakes in Peru, *Bull. Seismol. Soc. Am.* 80, 551–576.
- Fujii, Y., & Satake, K. (2012). Slip Distribution and Seismic Moment of the 2010 and 1960 Chilean Earthquakes Inferred from Tsunami Waveforms and Coastal Geodetic Data. *Pure and Applied Geophysics*, 170 (9-10), 1493–1509. doi:10.1007/s00024-012-0524-2
- Gibson, F. (1868). On the Wave Phenomena observed in Lyttelton Harbor, August 15, 1868. *Transactions and Proceedings of the New Zealand Institute*, 1, 195:196.
- Morris, B. and Borrero, J.C. (2014) Inundation of Whitianga town during the 1960 Chilean Tsunami, Waikato Regional Council Technical Report 2014/65, June 2014, ISSN 2230-4363 (Online)
- Power, W.L., & Gale, N. (2010). Tsunami Forecasting and Monitoring in New Zealand. *Pure and Applied Geophysics*, 168(6-7), 1125–1136. doi:10.1007/s00024-010-0223-9
- Power, W.L., Downes, G., & Stirling, M. (2007). Estimation of Tsunami Hazard in New Zealand due to South American Earthquakes. *Pure and Applied Geophysics*, 164(2-3), 547–564. doi:10.1007/s00024-006-0166-3

- Power, W.L., Wallace, L., Wang, X., & Reyners, M. (2011). Tsunami Hazard Posed to New Zealand by the Kermadec and Southern New Hebrides Subduction Margins: An Assessment Based on Plate Boundary Kinematics, Interseismic Coupling, and Historical Seismicity. *Pure and Applied Geophysics*, 169(1-2), 1–36. doi:10.1007/s00024-011-0299-x
- Prasetya, G. S., & Wang, X. (2011). *Tsunami frequency analysis for Eastern Coromandel and Waikato Region from Kermadec Trench and local sources within the Bay of Plenty* (No. 2011/135) (p. 65).
- Titov, V. V., & González, Frank, I. (1997). *Implementation and testing of the Method of Splitting Tsunami (MOST) model* (No. ERL PMEL-112) (p. 14). Retrieved from <http://www.pmel.noaa.gov/pubs/PDF/tito1927/tito1927.pdf>
- Titov, V. V., Moore, C. W., Greenslade, D. J. M., Pattiaratchi, C., Badal, R., Synolakis, C. E., & Kânoğlu, U. (2011). A New Tool for Inundation Modeling: Community Modeling Interface for Tsunamis (ComMIT). *Pure and Applied Geophysics*, 168(11), 2121–2131. doi:10.1007/s00024-011-0292-4
- Titov, V.V., and C.E. Synolakis (1995): Modeling of breaking and nonbreaking long wave evolution and runup using VTCS-2. *J. Waterways, Ports, Coastal and Ocean Engineering*, 121(6), 308–316.
- Titov, V.V., and C.E. Synolakis (1997): Extreme inundation flows during the Hokkaido-Nansei-Oki tsunami. *Geophys. Res. Lett.*, 24(11), 1315–1318.
- Wei, Y., Chamberlin, C., Titov, V. V., Tang, L., & Bernard, E. N. (2012). Modeling of the 2011 Japan Tsunami: Lessons for Near-Field Forecast. *Pure and Applied Geophysics*, 170(6–8), 1309–1331. <http://doi.org/10.1007/s00024-012-0519-z>